Ceramics International 49 (2023) 24428–24441

Contents lists available at ScienceDirect

Ceramics International

journal homepage: www.elsevier.com/locate/ceramint

# Preparation and characterization of Ce-MOF/g-$C_3N_4$ composites and evaluation of their photocatalytic performance

Zehra Durmus [a,*], Roberto Köferstein [b], Titus Lindenberg [a], Florian Lehmann [c], Dariush Hinderberger [c], A. Wouter Maijenburg [a,**]

[a] Centre for Innovation Competence (ZIK) SiLi-nano®, Institute of Chemistry, Martin Luther University Halle-Wittenberg, 06120, Halle (Saale), Germany
[b] Inorganic Chemistry, Institute of Chemistry, Martin Luther University Halle-Wittenberg, 06120, Halle (Saale), Germany
[c] Physical Chemistry, Institute of Chemistry, Martin Luther University Halle-Wittenberg, 06120, Halle (Saale), Germany

ARTICLE INFO

Handling Editor: Dr P. Vincenzini

*Keywords:*
Photocatalytic
Graphitic carbon nitride (g-$C_3N_4$)
Metal-organic framework (MOF)
Methylene blue
Dye degradation
Ce-BTC
Ce(1,3,5-BTC)$(H_2O)_6$

ABSTRACT

In this study, unique hybrid structures were constructed between a Ce-based metal-organic framework (Ce-MOF) and graphitic carbon nitride (g-$C_3N_4$) materials. In addition, the g-$C_3N_4$ materials used for these heterostructures were prepared by five different methods, namely the conventional pyrolysis method, chemical exfoliation by a strong acid, activation by an alkaline hydrothermal treatment, melamine-cyanuric acid supramolecular assembly with a mechanochemical method, and by the solvothermally pre-treated method. The structural and morphological properties of the resulting g-$C_3N_4$ sheets and their composites were characterized using scanning electron microscopy (SEM), X-ray diffraction (XRD), Fourier transform infrared spectrometry (FTIR), thermogravimetric analysis-derivative thermogravimetry (TGA-DTG), diffuse reflectance UV–vis spectroscopy (UV–vis DRS) and $N_2$ sorption-desorption isotherms (BET). Finally, the photocatalytic performance of the composites was determined by following the photocatalytic degradation of methylene blue (MB) in an aqueous solution under UV–visible light irradiation. It was found that the photocatalytic efficiency of the Ce-MOF/g-$C_3N_4$−TS composite was significantly higher than that of their counterparts (Ce-MOF or g-$C_3N_4$−TS) for the photocatalytic degradation of MB. When employing the composite, UV light-induced degradation of MB yielded an efficiency of 96.5% after 120 min for a dye solution containing 10 mg/L MB. This corresponds to a 5-fold or 2-fold improvement of the rate constant ($k$) when compared to the Ce-MOF or g-$C_3N_4$, respectively.

## 1. Introduction

The phenomena of global warming and greenhouse gas emissions as a result of the consumption of fossil-based energy sources and an increasing energy demand are among the most urgent problems emerging with modern technology. Sustainable, renewable and green solutions for the global energy supply will definitely reduce the environmental, ecological, social and economic side-effects of the current energy crisis. Solar energy is one of the alternative and emerging energy sources, which promises many advantages, such as renewable energy conversion and environmental pollution rehabilitation [1,2]. Many materials are being used for efficiently converting solar energy to electricity (in the form of photovoltaic devices or solar cells), but these systems are integrated by too many components, which makes them very costly. In addition, the intermittent nature of solar light hitting the earth requires new ways of storing solar energy for later use. To circumvent these disadvantages, photocatalysts can be considered as the heart of the next-generation systems for directly converting solar light into value-added solar fuels using a much simpler and cost-efficient system when compared to photovoltaic devices.

In particular, porous crystalline metal-organic frameworks (MOFs) synthesized from the coordination of metal nodes and organic bridging ligands are being investigated with increasing interest by researchers for their photocatalytic efficiency. Metal-organic frameworks (MOFs), which are commonly used as functional materials in many applications, such as gas separation [3], medicine [4], catalysis [5], sensors [6] and heat exchange [7], have also been employed in photocatalytic processes in recent years [8–10]. It has been suggested that MOFs exhibit a high potential in photocatalytic technologies due to their superior structural advantages, such as crystallinity [11], high porosity [12], structural

* Corresponding author.
** Corresponding author.
*E-mail addresses:* zehra.durmus@physik.uni-halle.de (Z. Durmus), wouter.maijenburg@chemie.uni-halle.de (A.W. Maijenburg).

https://doi.org/10.1016/j.ceramint.2023.01.063
Received 15 October 2022; Received in revised form 17 December 2022; Accepted 8 January 2023
Available online 10 January 2023

tunability [13] and diversified compound structure [14] when compared to conventional semiconductors. The application performance of different variations of MOFs depends on the selection and properties of the metal ion and the linker molecules used for the MOF synthesis. For instance, lanthanide ions are widely used in MOF structures, mainly due to their luminescence properties [15]. Furthermore, the maximum coordination numbers and flexible structural geometries of lanthanide ions, and the lanthanide contraction effect, create significant differences in the structural diversity of lanthanide (Ln)-based MOF structures [16,17]. In addition, Ln-based MOFs possess exceptionally high anisotropic magnetic moments due to the large number of different spins that are possible and a strong spin-orbit coupling [18]. All of these features make Ln-based MOFs very different from transition metal-based MOFs. Also the usage of aromatic carboxylate coordination compounds significantly contributes to the enhanced optical, magnetic and catalytic properties of this MOF family, due to their strong coordination capabilities and extended conjugation systems with multidentate structures.

Cerium (Ce), a member of the lanthanide family, possesses two main oxidation states. Diamagnetic Ce(IV) is a strong oxidant and is widely used in different catalyst structures [19,20]. It interacts well with many organic compounds [21,22], leading to Ce(III) compounds. Paramagnetic Ce(III) leads to compounds with unique magnetic [23,24] and luminescent features [25,26], which can be used for the synthesis of materials displaying magnetic ordering [27] or scintillation properties [28].

Besides these advantages and superior properties, MOFs also have some restrictions that limit their use in photocatalytic applications, such as low conductivity and stability, and large electron-hole pair recombination [29]. Therefore, various strategies should be applied to improve the photocatalytic application potential of these materials, such as the formation of a heterojunction with a narrow band gap semiconductor, the insertion of an amino group in the organic linker and/or the introduction of a MOF backbone [30]. As a promising semiconductor for the formation of a heterojunction, two-dimensional (2D) materials have received considerable attention for the development of more efficient photocatalysts with a high charge-carrier mobility coupled with a high current stability, thermal stability and conductivity [31]. 2D materials could be classified as a group of materials having layered structures including many organic, inorganic and hybrid materials, such as graphene, graphite, graphitic carbon nitride (g-$C_3N_4$), specific transition metal oxides, transition-metal-dichalcogenides (TMDs, such as $MoS_2$, $TiS_2$, $TaS_2$, $WS_2$, $MoSe_2$ and $WSe_2$) and other semiconductors [32–34]. What makes 2D photocatalysts different from other materials is their superior physical and chemical properties provided by their layered structure with a high specific surface area, which results from in-plane chemical bonds and van der Waals forces between the layers [32,35].

Particularly, g–$C_3N_4$–based photocatalysts have gained a considerable scientific and technical attention since Wang and coworkers first discovered the photocatalytic $H_2$ and $O_2$ evolution over g-$C_3N_4$ in 2009 [36]. g-$C_3N_4$ is composed of C and N atoms and can be easily produced with low-cost synthesis strategies. Its superior structural and physical properties, such as unique electric, optical, structural and physiochemical properties, make g–$C_3N_4$–based materials a new class of multifunctional nanoplatforms that can be used in different applications, for instance in different electronic, catalytic and energy applications. g-$C_3N_4$ is a metal-free photocatalyst with a band gap of 2.67 eV; herein, the conduction band minimum (CB) and the valence band maximum (VB) are located at approximately −1.42 V and 1.25 V vs. Ag/AgCl (pH 6.6), respectively [37]. In addition, g-$C_3N_4$ also possesses advantages of biocompatibility and non-toxicity.

g-$C_3N_4$ also has a few structural disadvantages that could limit its utilization in photocatalytic processes, such as fast recombination of electron–hole pairs, poor visible light absorption, its relatively small specific surface area when compared to other 2D materials, low intrinsic quantum efficiency and its inferior conductivity due to the presence of structural defects [38,39]. To overcome these inherent disadvantages, several functionalization routes for the modification of g-$C_3N_4$ have been suggested, including the regulation of the structural and electronic configuration of g-$C_3N_4$ and surface functionalization [40,41]. Furthermore, it is a well-known fact that heterogeneous photocatalytic reactions occur on the surface of photocatalyts, so therefore, various exfoliation and surface functionalization approaches have also been considered as effective strategies for enhancing the surface area of g-$C_3N_4$ [42–45].

Considering all these advantages and disadvantages related to the photocatalytic activities and the application potentials of both g-$C_3N_4$ and MOF-based materials, many researchers attempted to build heterojunctions or prepare composites by combining these materials in order to overcome the drawbacks and superimpose the advantages of these materials [46]. For instance, the MOF/g-$C_3N_4$ heterojunction can provide an enhanced surface area and separation of electron-hole pairs [38]. This heterojunction also enlarges the window of visible solar light absorption by providing a massive π-conjugated interaction between the aromatic ring of the MOF structure and the triazine rings of g-$C_3N_4$ [47]. This interaction is advantageous for an adequate electrostatic interaction at the surface, which supports the easy transfer of photo-generated charges through the heterojunction [48] in order to facilitate the sophisticated oxidation-reduction (redox) processes in which highly active radical species, such as hydroxyl (·OH) and superoxide anion ($O_2^-$) radicals, are formed. These radicals can then be used for the removal of organic pollutants, such as dyes, pharmaceuticals and pesticides, from various mediums using different methods [49,50]. The potential of the semiconductor-accommodated photocatalytic process is superior in water remediation due to advantages like chemical and photostability, synergistic oxidation power and superhydrophilicity [51–55]. The strong oxidant produced during these photocatalytic reactions can directly oxidize a compound in the medium or react with electron donors, such as water or hydroxide ions, to form hydroxyl radicals that react with the respective contaminants; often this reaction results in the desirable complete degradation of most known contaminants.

In this study, five different g-$C_3N_4$ structures were prepared by different synthesis methods, namely conventional synthesis, chemical exfoliation by a strong acid [56], activation by an alkaline hydrothermal treatment [57], melamine-cyanuric acid supramolecular assembly with a mechanochemical method [58,59] and melamine-cyanuric acid hydrogen-bonded supramolecular assembly by the solvothermally pre-treated method [60]. Various analytical techniques were applied to determine the structural and morphological distinctions between the physical and chemical characteristics among these g-$C_3N_4$ structures. Furthermore, Ce-MOF was in-situ synthesized by a hydrothermal reaction with and without g-$C_3N_4$, and the resulting composite structures were also fully characterized. Subsequently, the Ce-MOF/g-$C_3N_4$ heterostructure with the highest surface area and the lowest band gap was used as a photocatalyst for UV-light induced degradation of methylene blue (MB) in an aqueous solution to evaluate the photocatalytic performance of the composite structure. It should be noted here that we tested our photocatalysts under UV-light, because it has been reported that the band gap energy of MOFs is relatively high and therefore only a small portion of the solar spectrum can be absorbed by these materials, leading to their inability to provide a high catalytic efficiency under visible light [61]. On the other hand, it is also known that the photocatalytic efficiency of g-$C_3N_4$ is relatively low under visible light irradiation due to the high recombination rate of photogenerated electrons and holes. Structural and electronic interactions between MOF-type materials and g-$C_3N_4$ might reduce the band gap of their composites, but as the photocatalytic activity of such composite catalysts depends on many structural and experimental parameters, studies with visible light generally yield low catalytic efficiencies. Therefore, UV irradiation was preferred in this study to more precisely detect the catalytic activity of the composite structure compared to its counterparts.

## 2. Experimental details

### 2.1. Synthesis

#### 2.1.1. Preparation of graphitic carbon nitride (g-$C_3N_4$)

*g-$C_3N_4$* was prepared by the conventional pyrolysis of melamine. For this, melamine was heated to 550 °C in a muffle furnace (Carbolite P 310) with a heating rate of 2 °C $min^{-1}$ and kept at this temperature for 4 h. Afterwards, the resulting yellow bulk g-$C_3N_4$ was grounded into a powder.

*Protonated carbon nitride (g-$C_3N_4$–P)* was synthesized according to a previous report [62]. For this, a proper amount of melamine was dispersed into a diluted $H_2SO_4$ solution and stirred. Then, the suspension was placed into a Teflon-lined stainless-steel autoclave, which was heated to 180 °C and kept at this temperature for 12 h. Then, the acid-treated melamine precursor was cooled to room temperature and washed repeatedly with distilled water and ethanol. After drying at 80 °C for 12 h, the pale yellow g–$C_3N_4$–P powder was obtained by the same thermal procedure as defined above.

*Ammonium-based carbon nitride (g-$C_3N_4$–N)* was prepared by the mixing of melamine with ammonium chloride (1:5 w/w), after which the same thermal procedure as define above was applied. The resulting sample was a yellow powder.

*Mechanically treated carbon nitride (g-$C_3N_4$-TM)* was prepared by manually grinding melamine and cyanuric acid (with a molar ratio of 1:1) in a mortar for 30 min. Then, this mixture was exposed to the same thermal procedure as mentioned above, but this time in an Ar atmosphere. A pale-yellow product was obtained and denoted as g–$C_3N_4$–TM.

*Solvothermally treated carbon nitride (g-$C_3N_4$-TS)* was prepared by separately dissolving equal molar amounts of cyanuric acid and melamine into dimethyl sulfoxide (DMSO), which were vigorously stirred overnight at room temperature. Then, the solution containing cyanuric acid was added dropwise into the solution containing melamine and stirred afterwards for 8 h at room temperature. Then, the obtained white suspension was transferred to a Teflon-lined stainless-steel autoclave and heated to 180 °C and kept at this temperature overnight. The white precursor was centrifuged, washed repeatedly with distilled water and ethanol, and then dried at 120 °C for 8 h. Afterwards, this mixture was exposed to the same thermal procedure under Ar atmosphere as mentioned above and a pale-yellow product was obtained.

#### 2.1.2. Preparation of Ce-MOF

Ce-BTC was prepared at low temperature in an aqueous solution as reported in the literature [39,40]. In short, an aqueous solution containing 10 mmol/L $Ce(NO_3)_3{\cdot}6H_2O$ and a water-ethanol mixture (v/v = 1:1) containing 10 mmol/L 1,3,5-benzenetricarboxylic acid ($H_3BTC$) were mixed and separated into two solutions. Both of these solutions were heated for 1 h in a water bath at 60 °C; one of these solutions without stirring (in order to obtain a straw sheaf-like architecture) and the other solution with stirring (in order to obtain a rod-like architecture). In both cases, the final products formed white precipitates, which were washed repeatedly with ultrapure water and ethanol, and then dried in a vacuum oven at 60 °C for 12 h.

#### 2.1.3. Preparation of Ce-MOF/g-$C_3N_4$ composites

The Ce-MOF/g-$C_3N_4$ composites were prepared by the in-situ deposition of Ce-MOF nanoparticles onto the different g-$C_3N_4$ samples using the same procedure for the preparation of Ce-MOF with stirring, but in the presence of the pre-prepared g-$C_3N_4$ materials. The composite samples were denoted as Ce–CN, Ce–CN–P, Ce–CN–N, Ce–CN-TS and Ce–CN-TM as given Table 1.

### 2.2. Characterization studies

The chemical composition of all powders was determined by an X-ray diffractometer (XRD, Bruker D8 Advance, Cu-Kα, λ = 0.15406 nm, 40 kV, 40 mA) in the 2θ range of 5°–70° with a constant shutter speed, a time step of 0.5 s and a step size of ca. 0.01°. The software DiffracPlus EVA.Bruker was used for data evaluation and background correction.

**Table 1**
Nomenclature of g-$C_3N_4$ and Ce-MOF/g-$C_3N_4$ composites synthesized by different methods.

| Samples | Composites | Precursor | Pre-treatment | Post-treatment |
|---|---|---|---|---|
| g-$C_3N_4$ | Ce–CN | melamine | – | – |
| g–$C_3N_4$–P | Ce–CN–P | melamine | – | $H_2SO_4$ |
| g–$C_3N_4$–N | Ce–CN–N | melamine | $NH_4Cl$ | – |
| g–$C_3N_4$–TM | Ce–CN–TM | melamine + CYA | grinding | – |
| g–$C_3N_4$–TS | Ce–CN–TS | melamine + CYA | mixing in DMSO | – |

g-$C_3N_4$: graphitic carbon nitride, Ce: Ce-MOF, CYA: cyanuric acid.
$NH_4Cl$: ammonium chloride, DMSO: dimethyl sulfoxide, $H_2SO_4$: sulfuric acid.

Chemical characterization of the functional groups in the samples was obtained with a Fourier transform infrared (FTIR) spectrometer (Tensor 27, Bruker Co.) equipped with a diamond-ATR unit in the wavenumber range of 4000–250 $cm^{-1}$.

The morphology of the samples was investigated by a scanning electron microscope (SEM, Carl Zeiss Merlin).

The specific surface area was determined using nitrogen five-point Brunauer-Emmett-Teller (BET) method (Nova 1000, Quantachrome Corporation).

The UV–vis diffuse reflection spectrum (DRS) of the samples was recorded by a UV–Vis diffuse reflectance spectrometer (Agilent, Cary 60) in the wavelength range of 200–800 nm $BaSO_4$ was used as the substrate and the obtained reflectance spectra were converted to absorbance spectra by the Kubelka–Munk method.

Thermal properties of the samples were obtained by thermal gravimetric analysis -derivative thermogravimetry (TGA-DTG) measurements in flowing air with a heating rate of 10 K/min using a Netzsch Jupiter STA 449F5.

Elemental analysis was also performed to determine the chemical composition of the samples using of the elements CHNS–O Analyzer (EA 3000).

The continuous-wave electron paramagnetic resonance (CW EPR) analysis was achieved using a Bruker A300-10/12 spectrometer at room temperature. All EPR spectra were measured using a Miniscope MS 5000 (Magnettech GmbH, Berlin, and Freiberg Instruments, Freiberg, Germany), an MS 5000 temperature controller (Magnettech GmbH, Berlin, Germany) and Freiberg Instruments software. The samples were directly exposed to light inside the EPR spectrometer using a fiber-coupled multi-wavelength LED light source (Prizmatix Ltd., Cholon, Israel). The EPR spectra were integrated to obtain the microwave absorption spectra. The baseline around the signal was fitted with a 4th-order polynomial t. Then, the double integral (DI) was calculated from the baseline-corrected microwave absorption spectra. Each DI had an allocated value for irradiation time. Since one measurement took 10 min and the sample showed a small structural change during irradiation, this time value is the average of starting point and end point of the measurement.

Dye degradation experiments were performed to compare the photocatalytic performances of Ce-MOF, g-$C_3N_4$ and a Ce-MOF/g-$C_3N_4$ composite in the UV-light driven degradation of methylene blue (MB). For this, 25 mg of the respective catalyst was dispersed in 100 mL of an aqueous solution containing 10 mg/L MB. This catalyst-suspended dye solution was first stirred at 250 rpm for 30 min in the dark to allow the physical adsorption of dye molecules onto the catalyst surface. Then, the solution was stirred under UV light for 120 min. At specific intervals (after 10, 20, 30, 45, 60, 75, 90 and 120 min), 2 mL of the sample was taken from the mixture and quickly centrifuged at 10,000 rpm for 1 min. Finally, the concentration of the remaining dye in the solution was determined by scanning the supernatant in the wavelength range of

200–800 nm with the UV–vis spectrophotometer and by following the characteristic peak of MB at 665 nm at various intervals.

The regeneration of the hybrid Ce-MOF/g-$C_3N_4$ catalyst was investigated by a typical reusability test [63]. For this, 25 mg of Ce-MOF/g-$C_3N_4$ was isolated from the reaction medium by filtration. The isolated Ce-MOF/g-$C_3N_4$ was then washed with water and ethanol several times to remove adsorbed dye residues from the surface of the catalyst. Then, the catalyst was dried and used again for the photodegradation of MB as described above.

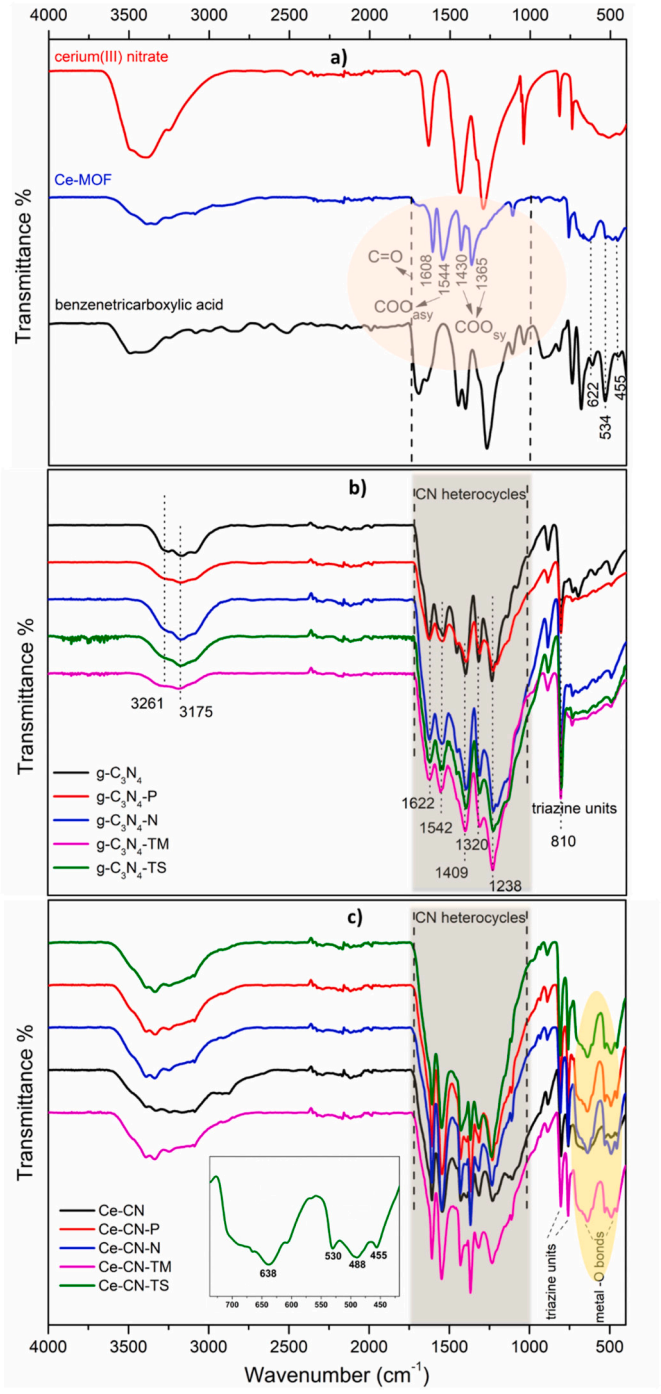


**Fig. 1.** FTIR spectra of **a)** Ce-MOF and its precursors, **b)** g-$C_3N_4$ samples synthesized with different methods and **c)** Ce–CN composites.

## 3. Results and discussion

### 3.1. Structural characterization

The FTIR spectra of the obtained Ce-MOF and its precursors are presented in Fig. 1a. The spectra of benzenetricarboxylic acid and Ce-

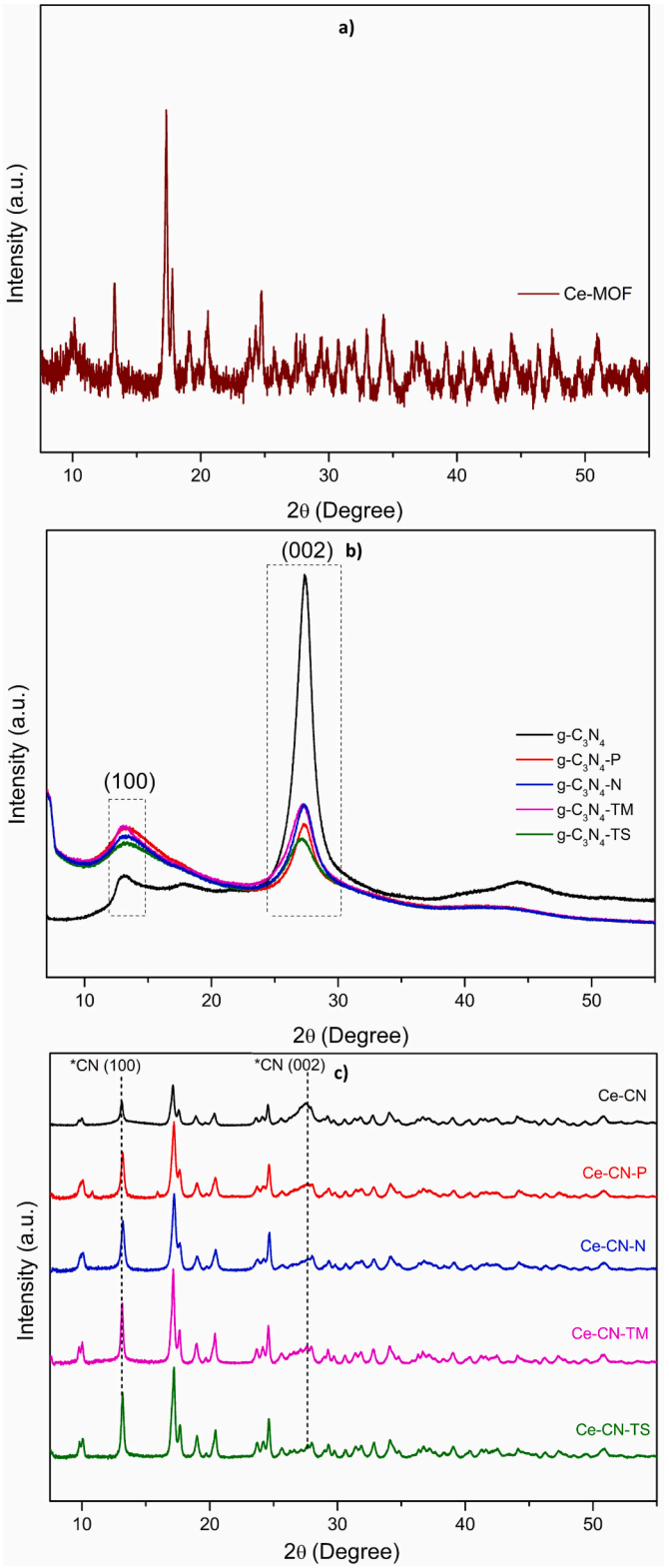


**Fig. 2.** XRD patterns of **a)** Ce-MOF, **b)** g-$C_3N_4$ samples synthesized with different methods and **c)** the corresponding Ce–CN composites.

MOF both show the characteristic bands at 1608 $cm^{-1}$, which belongs to $\nu_{asy}$-asymmetric vibration, and at 1430 and 1365 $cm^{-1}$, which both belong to $\nu_{sy}$-symmetric vibrations of $COO^-$ groups. In addition, small peaks can be observed in Fig. 1a and c between 450 and 700 $cm^{-1}$ (at 622, 534 and 455 $cm^{-1}$) corresponding to Ce–O stretching vibrations of the Ce-MOF sample. Furthermore, it is known that the region between 800 and 1300 $cm^{-1}$ is the fingerprint region of terephthalic acid, corresponding to out-of-plane vibrations. The broader peak observed at 3400–3300 $cm^{-1}$ is attributed to the stretching vibrations of $OH^-$, which indicates physically bonded water molecules on the surface of the Ce-MOF crystals and all other samples [64].

The FT-IR spectra of all g-$C_3N_4$ samples synthesized with different methods show several characteristic peaks related to the chemical bonding between carbon and nitrogen, as can be clearly seen in Fig. 1b [65]. The strong absorption band in the range of 1650–1200 $cm^{-1}$ is assigned to the typical skeletal stretching vibrations of s-triazine or tri-*s*-triazine. The peak at 1622 $cm^{-1}$ corresponds to the C–N stretching vibration mode, while the peaks observed at 1238, 1320 and 1409 $cm^{-1}$ are associated with the C–N heterocycle stretching of g-$C_3N_4$ [66]. The sharp peak observed in the spectra of all g-$C_3N_4$ samples at 808 $cm^{-1}$ is a characteristic out-of-plane bending vibration mode of the triazine units [67,68]. The broad adsorption band at 3000–3300 $cm^{-1}$ and two weak stretching bands at 2927 and 2769 $cm^{-1}$ are assigned to adsorbed water molecules, C–H stretching and N–H stretching, respectively [69].

The FTIR spectra of the composites are similar to their g-$C_3N_4$ counterparts. This result indicates that the C–N bond lengths of the g-$C_3N_4$ samples were not changed upon introduction of the MOF. It was also observed that the characteristic peaks of the g-$C_3N_4$ structure were enhanced in the composites, which implies a certain interaction between g-$C_3N_4$ and the MOF [70].

Fig. 2 shows the X-ray diffraction patterns of the pure Ce-MOF, the g-$C_3N_4$ samples synthesized by different methods and the Ce-MOF/g-$C_3N_4$ composites. The characteristic peaks of the Ce-based MOF structure are in the 2θ range of 5–50° in Fig. 2a, which corresponds to the reported XRD data of the Ce(1,3,5-BTC)$(H_2O)_6$ MOF. The sharp peaks indicate the crystalline nature of the synthesized pure Ce-MOF and the Ce-MOF/g-$C_3N_4$ composites [71,72].

It is well known that g-$C_3N_4$ is constructed based on tri-*s*-triazine building blocks. In accordance, the XRD patterns of all g-$C_3N_4$ samples synthesized by the different methods (Fig. 2b) and also the Ce–CN samples (Fig. 2c) feature two pronounced diffraction peaks at 27.34° and 13.05° attributed to the typical interplanar stacking of the conjugated aromatic tri-*s*-triazine building blocks, as documented in the Joint Committee on Powder Diffraction Standards (JCPDS) database (87–1526) [73]. The peak at 27.34° with a high intensity represents the characteristic (002) inter-planar graphitic stacking. It was found that the intensity of the (002) peak was significantly decreased in g-$C_3N_4$ samples synthesized with different methods when compared to the bulk g-$C_3N_4$, which suggests an exfoliated morphology and destroyed interlayer structure of the g-$C_3N_4$ sheets after successful treatment or due to the applied synthesis methods [57–60,62,74]. Another peak observed at 13.05°, indexed as (100), is related to an inter-planar separation of repeating motif, like the hole-to-hole distance of the continuous tri-*s*-triazine pores that represent the periodic arrangement of the condensed tri-*s*-triazine units in the sheets, which is consistent with g-$C_3N_4$ reported in the literature [75].

When taking a closer look at Fig. 2b, it can be seen that the (002) peaks of g–$C_3N_4$–TS, g–$C_3N_4$–TM and g–$C_3N_4$–P shifted to 27.14°, 27.21° and 27.33°, respectively, compared to g-$C_3N_4$ and g–$C_3N_4$–N (27.37°). Especially, the (002) plane of the g–$C_3N_4$–TS sample showed a larger shift (27.14°), which reveals an increase in the interlayer distance and enlarged in-plane nitride pores in the g–$C_3N_4$–TS structure [76]. Compared with the g-$C_3N_4$ sample, it was observed that the (002) diffraction peak of the g–$C_3N_4$–P sample decreased, which could be attributed to the fact that the strong acidification treatment partially destroys the graphitic structure and produce some fragments in the g–$C_3N_4$–P sample. In addition, it was also found that the introduction of $NH_4Cl$ into the g-$C_3N_4$ structure resulted in a decreased intensity of the characteristic (100) peak at 13.0°. This was due to the inhibition of $NH_3$ formation by the decomposition of $NH_4Cl$ during the polycondensation reaction of heptazine as reported before [57]. The presence of cyanuric acid in the g–$C_3N_4$–TS and g–$C_3N_4$–TM samples might have resulted in a disturbance of the graphitic structure through partial substitution of N by C in the matrix [37], which thus altered the in-plane structural repeating network [66,77]. This phenomenon can be attributed to the packing disturbance and single layer undulation caused by the introduction of the nitrogen dopant [78]. Furthermore, both the (001) and (002) peaks slightly shifted towards lower angles with a significant broadening and a slight decrease in the intensity for g–$C_3N_4$–TM and g–$C_3N_4$–TS prepared with both melamine and cyanuric acid at a molar ratio of 1:1. This slight shift of these peaks indicate an increase in the in-plane nitride pores and the interlayer distance within the conjugated aromatic system [79].

While the intensity of the (001) peak was low in the g-$C_3N_4$ samples synthesized by different methods, its intensity became higher in the Ce-MOF/g-$C_3N_4$ composites as it overlapped with one of the characteristic peaks of the Ce-MOF at the same position (Fig. 2c).

Table 2 shows the results of the elemental analysis of the g-$C_3N_4$ samples synthesized by different methods. The C/N atomic ratio of the g-$C_3N_4$ samples varied in the range of 0.64–0.66, which is lower than the theoretical value of 0.75, with g–$C_3N_4$–TS exhibiting the highest C/N atomic ratio. However, these values are consistent with the literature as Akaike et al. reported a C/N atomic ratio of 0.67 corresponding to the composition of melon [80]. Furthermore, Miller et al. also obtained a C/N ratio of 0.67 using an annealing process at 600 °C [81]. It is worth to note that the highest amount of oxygen was found for g–$C_3N_4$–N, which is probably due to oxygenated carbon (C═O) as a result of an incomplete polymerization during the formation of g-$C_3N_4$ [82]. This sample also contained the highest amount of hydrogen. The lowest amount of oxygen was obtained for the g–$C_3N_4$–TS sample, which indicates a higher degree of polymerization in the graphitic nitride structure. Furthermore, the small differences in atomic composition among the g-$C_3N_4$ samples could be originated from a small amount of residual groups on the surface, which contain H and O and therefore may be ascribed to $NH_2$/NH groups and adsorbed $CO_2$, $O_2$ and $H_2O$ [83].

Table 2 also presents the BET surface areas of all g-$C_3N_4$ samples. The

**Table 2**
Elemental analysis and the obtained BET surface area of the g-$C_3N_4$ samples synthesized with different methods.

| Sample | Elemental composition | | | | C/N atomic ratio | $S_{BET}$ ($m^2$/g) |
|---|---|---|---|---|---|---|
| | C (wt%) | H (wt%) | N (wt%) | O (wt%) | | |
| g–$C_3N_4$ | 34.09 | 1.78 | 61.67 | 2.46 | 0.644 | 21 |
| g–$C_3N_4$–N | 33.44 | 2.11 | 59.95 | 4.50 | 0.650 | 41 |
| g–$C_3N_4$–P | 34.12 | 1.91 | 60.69 | 3.28 | 0.650 | 25 |
| g–$C_3N_4$–TM | 34.60 | 0.92 | 61.66 | 2.82 | 0.640 | 9 |
| g–$C_3N_4$–TS | 34.98 | 1.79 | 62.14 | 1.07 | 0.660 | 83 |

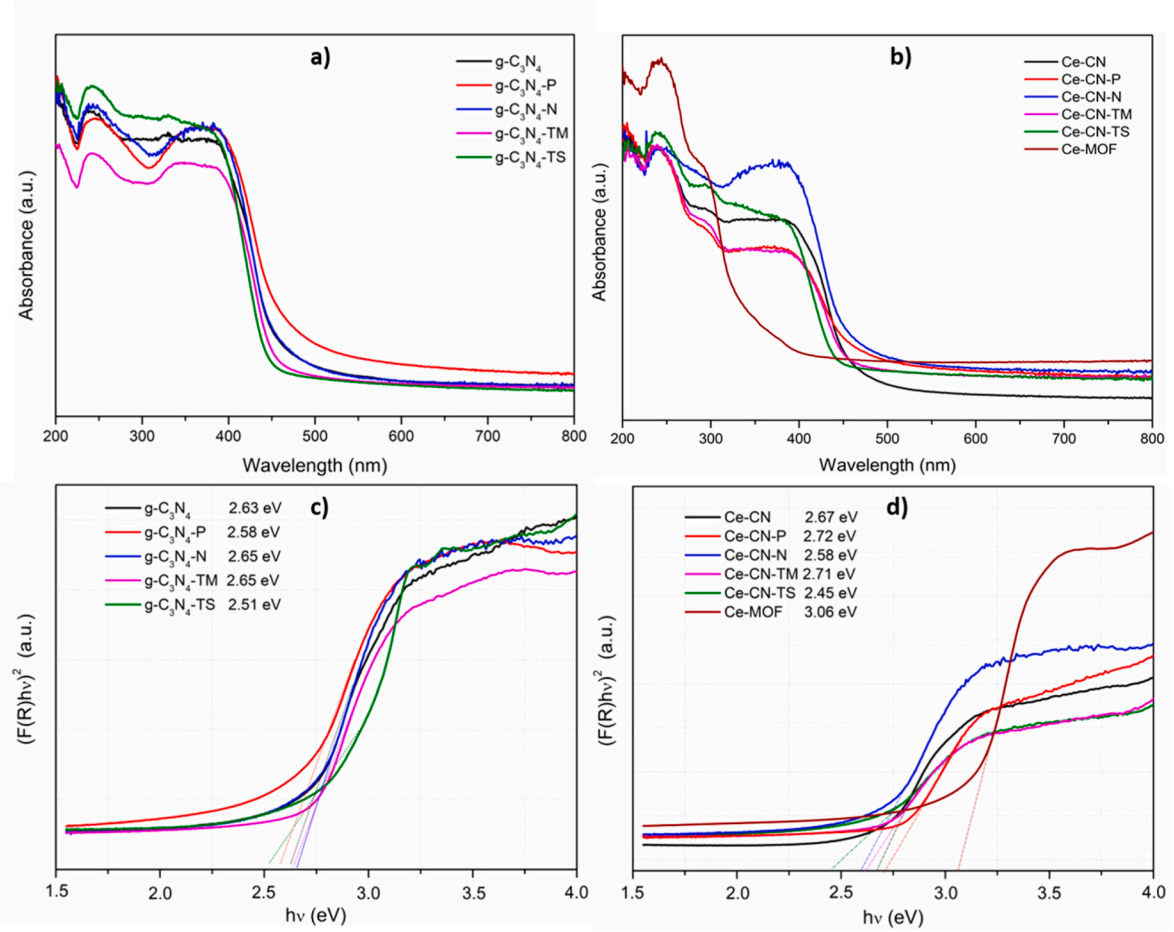


**Fig. 3.** UV–Vis DRS (a,b) and Tauc (c,d) plots of the **a, c)** g-$C_3N_4$ and **b, d)** Ce-MOF and Ce–CN samples.

BET surface areas of g–$C_3N_4$–N and g–$C_3N_4$–TS were calculated to be 41 and 83 $m^2$/g, respectively, which are much higher than those of g-$C_3N_4$ (21 $m^2$/g), g–$C_3N_4$–P (25 $m^2$/g) and g–$C_3N_4$–TM (9 $m^2$/g). It is clear that the bulk g-$C_3N_4$ displays a low specific surface area, which is consistent with the previously reported result [84], and could be attributed that the mechanical mixing of the precursors (melamine and cyanuric acid)

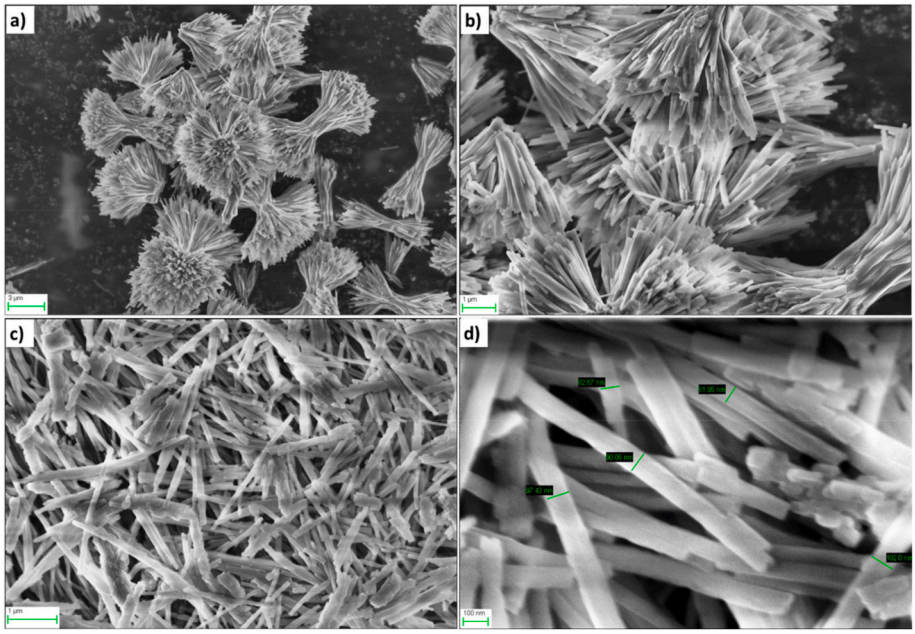


**Fig. 4.** Ce-MOF structures: **a, b)** straw sheaf like and **c, d)** rod-like architectures obtained without and with vigorous stirring, respectively.

inhibiting the polymerization of graphitic nitride in g–$C_3N_4$–TM. It is expected that the sample with the highest surface area (g–$C_3N_4$–TS) is favorable for catalyzing the photoreaction by facilitating an enhanced mass transfer and increasing the number of active sites [85,86].

The optical properties of Ce-MOF, g-$C_3N_4$ synthesized by these different methods and of the Ce–CN composites were investigated by UV–Vis diffuse reflectance spectroscopy (DRS) as illustrated in Fig. 3a and b, respectively. The band gaps of these semiconductor photocatalysts were estimated by transformation of the DRS spectra into a Tauc plot using the following equation:

$$F(R)hv = A\left(hv - E_g\right)^{n/2}$$

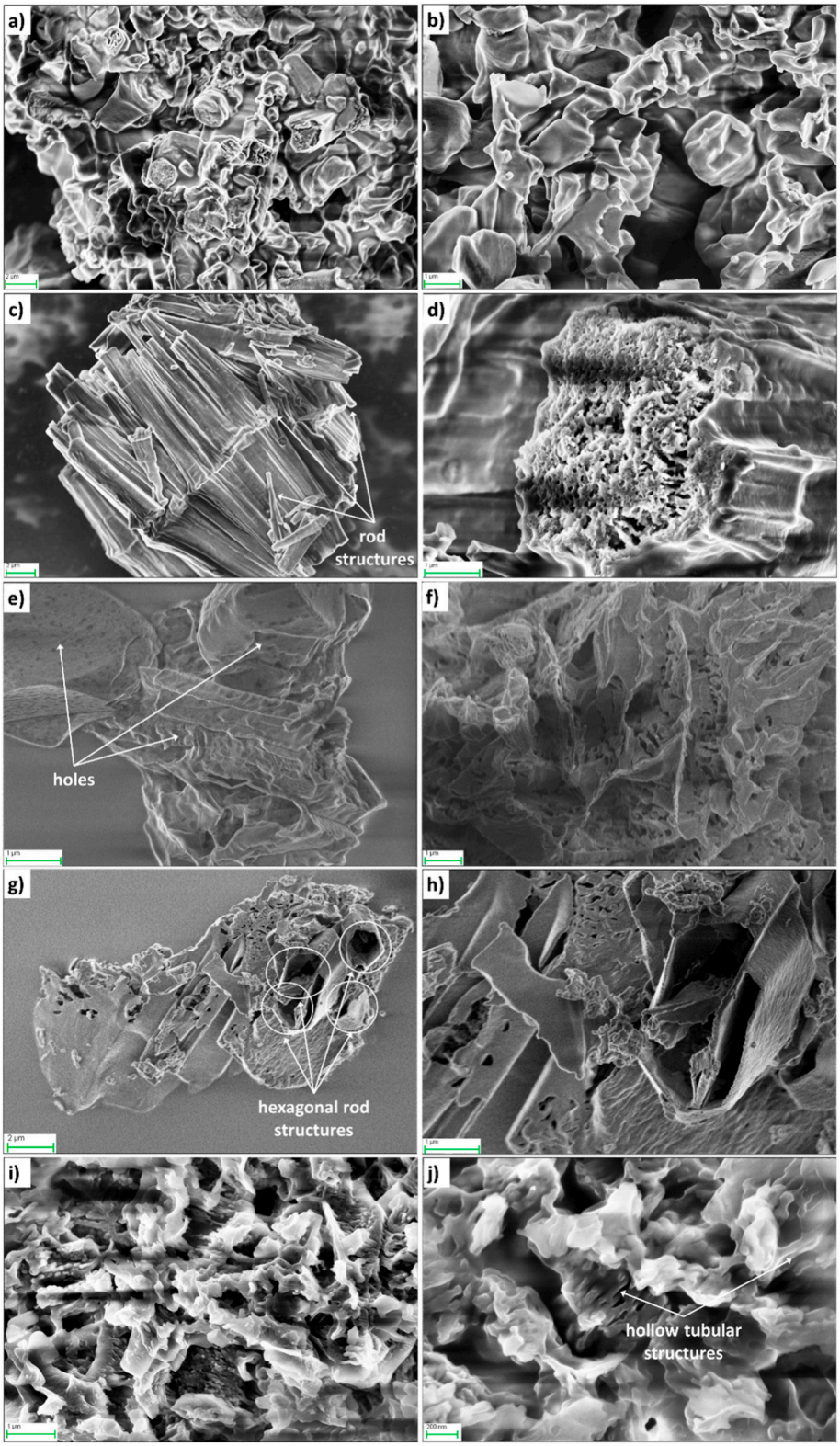


**Fig. 5.** SEM images of **a, b)** g-$C_3N_4$, **c, d)** g–$C_3N_4$–P, **e, f)** g–$C_3N_4$–N, **g, h)** g–$C_3N_4$–TM and **i, j)** g–$C_3N_4$–TS.

where A is a proportionality constant (usually 1), h is the Planck constant, υ is the optical frequency and $E_g$ is the band gap. In this equation, n is determined by the type of optical transition within the semiconductor. As g-$C_3N_4$ is a semiconductor with an indirect transition, n is taken as 4 [87]. The corresponding Tauc plots of these samples are given in Fig. 3c and d. The band gap energies ($E_g$) of the g-$C_3N_4$ samples synthesized by different methods and of the Ce–CN samples are calculated to be in the range of 2.51–2.65 eV and 2.45–2.75 eV, respectively. Among the pure g-$C_3N_4$ samples, the lowest band gap belongs to the g–$C_3N_4$–TS sample (2.51 eV), which is also the sample with the highest BET surface area. Among the composites, Ce–CN-TS also yielded the lowest band gap (2.45 eV). This low $E_g$ value indicates that Ce–CN-TS promises the highest visible light harvesting capability needed to produce more photogenerated charge carriers [88].

The morphologies and microstructural features of two different Ce-MOF samples (prepared with and without stirring), the g-$C_3N_4$ samples synthesized by different methods and the Ce-MOF/g-$C_3N_4$ composites were investigated by SEM analysis (Figs. 4–6). When synthesizing the Ce-MOF without stirring, the resulting nanostructure exhibits a straw-sheaf like morphology formed by the aggregation of nanorods (Fig. 4a and b). This structure consists of a bundle of outspread nanorods radially arranged from the center [89]. Fig. 4c and b shows typical rod-like Ce-MOF structures obtained by the same method, but with stirring. The length of these rod-like Ce-MOF nanostructures ranged from sub-micrometer to a few micrometers with relatively high aspect ratios and smooth surfaces [90,91].

In Fig. 5, the different morphologies of the obtained g-$C_3N_4$ structures with different synthesis methods can be seen. As shown in Fig. 5a and b, the g-$C_3N_4$ sample displays bulky aggregated g-$C_3N_4$ sheets with numerous wrinkles. These aggregated particles have an average size of several micrometers and a wide size distribution. The morphology of g–$C_3N_4$–P turned to aggregates of nanorods with a diameter of 80–100 nm and a length of 200–400 nm (Fig. 5c, and d). The size of these g–$C_3N_4$–P rods is much smaller than that of bulk g-$C_3N_4$, which is consistent with the increase in BET surface area as shown in Table 2. When g-$C_3N_4$ was synthesized by introducing $NH_4Cl$ (g–$C_3N_4$–N), its morphology turned into a paper wad-like structure with a uniform hole structure with a size of ~40–60 nm as shown in Fig. 5e and f. The formation of these mesopores is likely due to the corrosion effect of $NH_4Cl$ on the layered g-$C_3N_4$ structure during the hydrothermal synthesis [92]. Decomposition of $NH_4Cl$ during the calcination process produces a large amount of $NH_3$ and thus inhibits the polycondensation reaction of heptazine units [57]. The porous structures observed in these SEM images is also consistent with the obtained larger surface area of this sample (Table 2). For g–$C_3N_4$–TM, the large and thick slabs of nanosheets exhibiting rods with a length of 3–5 μm (Fig. 6g and h) reveal that the rod structures are composed of multiple two-dimensional graphene-like nanosheets. But interestingly, this structure showed a low surface area value according to the BET analysis. Guo and coworkers [44] explained this by mentioning that the melamine and cyanuric acid are held together in the same plane by multiple hydrogen bonds, which yielded the hexamer (rosette) structure. These hexamers can then be laterally arranged in two dimensions to form planar sheets, which are stacked in three dimensions to result in the observed channels [93]. These two morphologies, hollow sheets and short nanorods, were also observed for g–$C_3N_4$–TS prepared by using the cyanuric acid-melamine complex as a starting material assisted by the molecular self-assembly in DMSO. However, in this case a much higher surface area of 83 $m^2/g$ was obtained (Table 2).

The distribution of Ce-MOF nanoparticles in the Ce-MOF/g-$C_3N_4$ composites, in which the majority of the morphologically different g-$C_3N_4$ structures are covered or decorated with the scattered MOF nanoparticles can be seen in Fig. 6. Although the synthesis procedure with stirring was applied for the synthesis of the Ce-MOF part in all Ce-MOF/g-$C_3N_4$ composites, it can be observed from the SEM pictures that

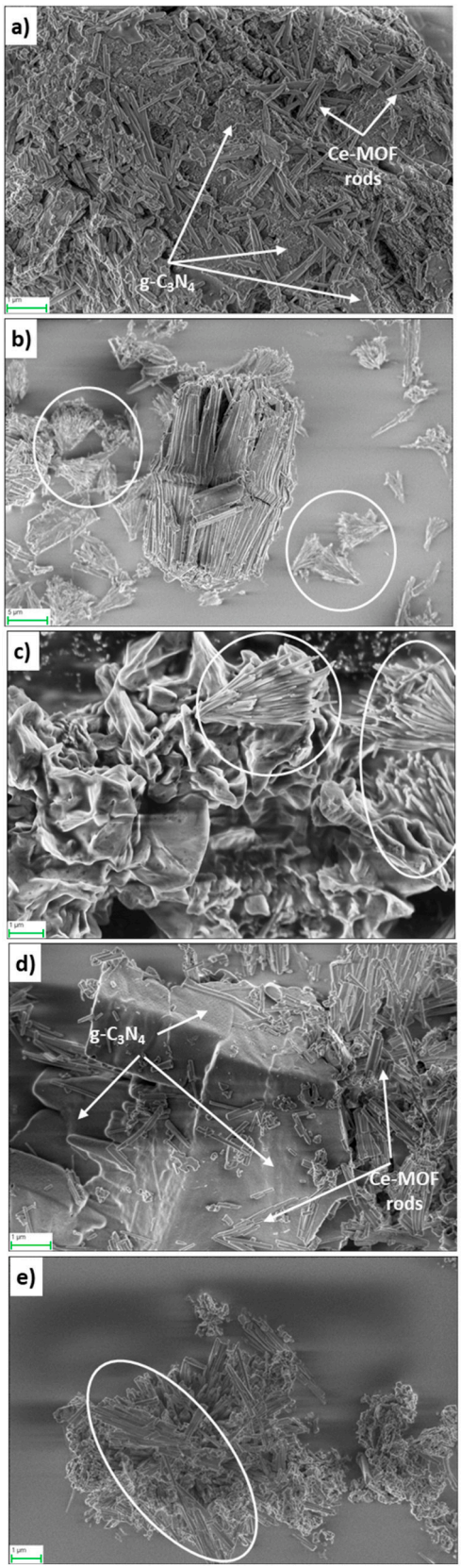


**Fig. 6.** SEM images of the composite structures: **a)** Ce–CN, **b)** Ce–CN–P, **c)** Ce–CN–N, **d)** Ce–CN–TM and **e)** Ce–CN–TS. Please note that the circles highlight Ce-MOF structures.

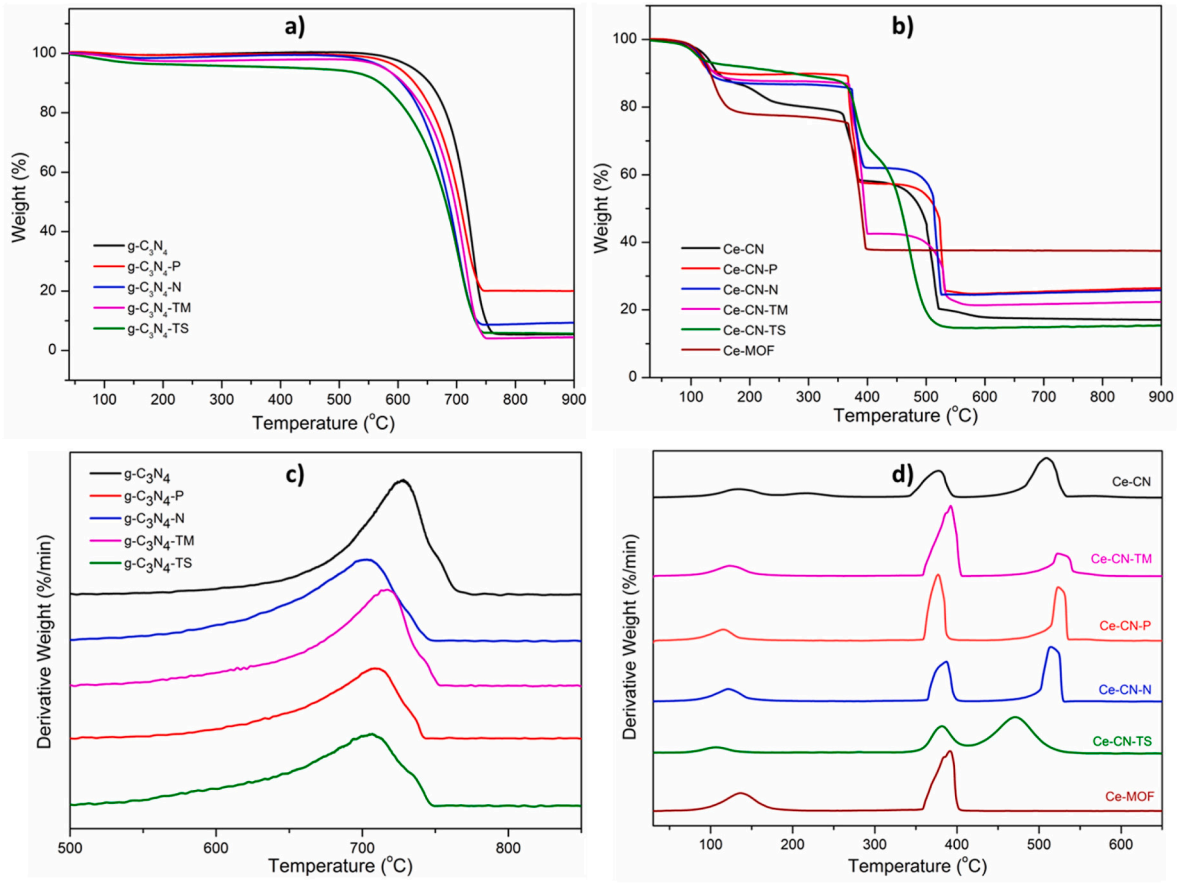


**Fig. 7.** TGA and DTG (derivative thermogravimetry) thermograms of **a, c)** g-$C_3N_4$ and **b, d)** Ce-MOF and Ce–CN samples.

some composites include rod-like structured Ce-MOF, some straw-like Ce-MOF and others contain both architectures. The Ce-MOF nanoparticles can be clearly observed as anchors like rods and/or straw sheaf-like structures, which are located both on the inside and on the outside of the porous g-$C_3N_4$ materials.

Fig. 7 demonstrates the TGA and DTG thermograms of the different g-$C_3N_4$ samples (a,c) and of the Ce-MOF/g-$C_3N_4$ composites (b,d). All g-$C_3N_4$ samples showed a single-step decomposition around 700 °C, with a slight additional weight loss in the temperature range of 20–200 °C corresponding to the removal of physically adsorbed water. It was found that the decomposition of all g-$C_3N_4$ samples was finished in the range of 700–750 °C, which is consistent with Gillan's report [94,95]. After full decomposition, almost all g-$C_3N_4$ samples had a residue of approximately 5 wt%, except for g–$C_3N_4$–P. The higher amount of residue obtained for g–$C_3N_4$–P might be attributed to the capturing of oxygen from the air by the protonated surfaces during the heating and pyrolysis process.

In the TGA curves of the Ce–CN composites, the first weight loss step in Fig. 7b probably originates from adsorbed water as well as absorbed water inside the MOF structure, resulting in a larger weight loss when compared to the bare g-$C_3N_4$ samples. The second weight loss step refers to the decomposition of the Ce-MOF structure, since the pure g-$C_3N_4$ samples did not have any significant weight loss in this temperature range (300–420 °C). In this temperature range, all composite samples exhibited a rapid weight loss of 24–36% accompanied by the formation of $CeO_2$. In addition, it was found that the complete decomposition of the composite structures is already finished at approximately 530 °C, after the third weight loss step in Fig. 7b and d, whereas the pure g-$C_3N_4$ samples are not completely decomposed until temperatures higher than 700 °C are reached. As it is a well-known fact that any metals present in an organic/inorganic hybrid material can act as catalysts for enhancing the degradation rate of the organic compounds and/or polymers at high temperatures, it could be concluded that the Ce from the metal organic framework may catalyze the degradation of the g-$C_3N_4$ structures. Consequently, the degradation of the composites finishes approximately 200–250 °C earlier than that of the pure g-$C_3N_4$.

The EPR spectra of Ce-MOF, g–$C_3N_4$–TS and Ce–CN-TS during irradiation with blue light are shown in Fig. 8a, b and 8c, respectively. The radical concentration of all samples, depicted as the double integral (DI) in Fig. 8d, increases to a maximum plateau within the first 30 min of irradiation. Ce-MOF shows almost no EPR signal, since the unpaired electrons in this experiment are generated by breaking bonds in the huge conjugated system of g-$C_3N_4$, resulting in the formation of biradicals, which is not available in the MOF. The Ce–CN-TS composite shows the highest radical concentration before and after irradiation, despite partly consisting of the EPR-inactive MOF material. During irradiation with blue light, the radical concentration increases by 85.9% in Ce–CN-TS and 77.9% in g–$C_3N_4$–TS. Therefore, we can conclude that the g-$C_3N_4$ structure in the composite material is more accessible for photons than the pure g-$C_3N_4$.

### 3.2. *Analysis of the photocatalytic activity of Ce-MOF, g-$C_3N_4$ and their composite for organic dye degradation*

It is generally accepted that the hierarchical porous structure of a photocatalyst could possess a higher light-harvesting capacity and provide more active sites for the photocatalytic reactions to take place [96]. Additionally, photocatalysts with a smaller band gap should be able to absorb a larger part of the solar spectrum [97]. In the previous section, it was shown that g–$C_3N_4$–TS has the highest surface area and the lowest band gap energy (2.51 eV) among the different g-$C_3N_4$ samples synthesized within this study. Additionally, the Ce–CN-TS composite also

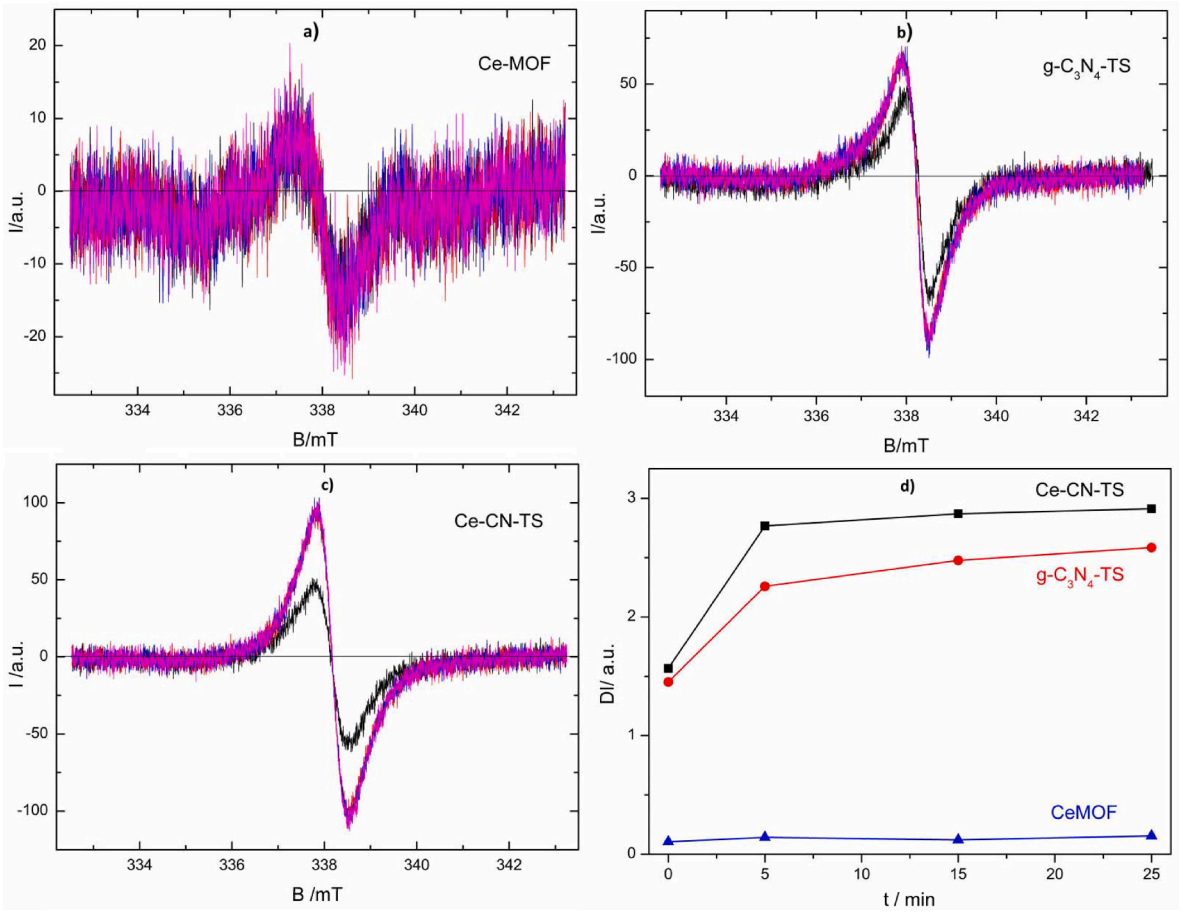


**Fig. 8.** EPR spectra of **a)** Ce-MOF, **b)** g–$C_3N_4$–TS and **c)** Ce–CN-TS during irradiation at t = 0 min (black), 5 min (red), 15 min (blue) and 25 min (magenta), and **d)** double integral (DI) during blue light irradiation normalized to the weight of the samples. (For interpretation of the references to color in this figure legend, the reader is referred to the Web version of this article.)

showed the lowest band gap energy (2.45 eV) among all composites. Based on these structural and light absorption properties of the materials examined in this work, Ce-MOF, g–$C_3N_4$–TS and Ce–CN-TS were selected to be used as photocatalysts in the UV-light-driven dye degradation experiments, so that the photocatalytic performance of such materials can be compared. The resulting UV–vis absorption spectra of the dispersions containing Ce-MOF, g–$C_3N_4$–TS or Ce–CN-TS in an aqueous methylene blue (MB) solution are given in Fig. 9, together with the chemical structure of MB and a photograph of the resulting suspensions containing Ce–CN-TS after 30 min, 60 min and 120 min of dye degradation. It should be noted that a blank experiment without solid catalyst was not performed, because Lei and coworkers reported that a slight discoloration (~10%) occurred within 120 min in absence of any catalyst. Therefore, they implied that MB was quite stable under visible light irradiation [98].

As can be seen from these UV–vis spectra, all photocatalysts were able to decompose MB as observed by the decrease in the intensity of the MB absorption peak as a function of irradiation time. To investigate the kinetics of the dye degradation, these UV–vis spectra were converted to the respective relative change in dye concentration ($C/C_0$) as given in Fig. 10a. It was found that the Ce-MOF yielded a moderate decrease in dye concentration (~40% after 2 h), whereas g–$C_3N_4$–TS performed significantly better (~70% after 2 h). However, the Ce–CN-TS composite was able to almost completely decompose MB (~96.5% after 2 h). These results could be further quantified by applying a kinetic equation. In the literature, it is generally accepted that the photocatalytic degradation of dye molecules can be expressed with the following first-order or pseudo first-order kinetic equations [99]:

$$C_t = C_0 e^{-kt}$$

$$ln\left(\frac{C_t}{C_0}\right) = -kt$$

where $C_0$ and $C_t$ are the initial dye concentration and the concentration at time $t$, respectively, and $k$ is the rate constant ($min^{-1}$). The pseudo first-order equation is the simplified version of the Langmuir-Hinshelwood kinetic model for low concentrations. The plot of $ln(C_t/C_0)$ versus $t$ yields straight lines (Fig. 10b) and the slopes of these lines represent the rate constants, which are listed as an inset in Fig. 10b. Accordingly, the rate constants were found to be $5{\cdot}10^{-3}$, $11.2{\cdot}10^{-3}$ and $24.5{\cdot}10^{-3}$ $min^{-1}$ for the Ce-MOF, g–$C_3N_4$–TS and Ce–CN-TS, respectively. This dye degradation study clearly indicates that the composite structure has an enhanced photocatalytic efficiency when compared to Ce-MOF and g-$C_3N_4$. Regarding the experimental conditions in this work, the rate constant ($k$) of the composite was improved approximately 5-fold and 2-fold with respect to the Ce-MOF and g-$C_3N_4$, respectively.

The Ce–CN-TS composite studied in this work yielded a similar rate constant as found in the literature for a different MOF. For instance, Lei et al. prepared and characterized the hybrid g-$C_3N_4$/MIL88B(Fe) by exfoliating bulk g-$C_3N_4$ as carbon nitride nanosheets (CNNSs), which were coupling with MIL-88B(Fe) [98]. They reported that the hybrid containing 6% of CNNSs exhibited the highest photocatalytic activity for the degradation of MB based on their photoluminescence spectra, electrochemical measurements and photocatalytic experiments. The rate constant ($k$) of their g-$C_3N_4$/MIL88B(Fe) hybrid was reported to be

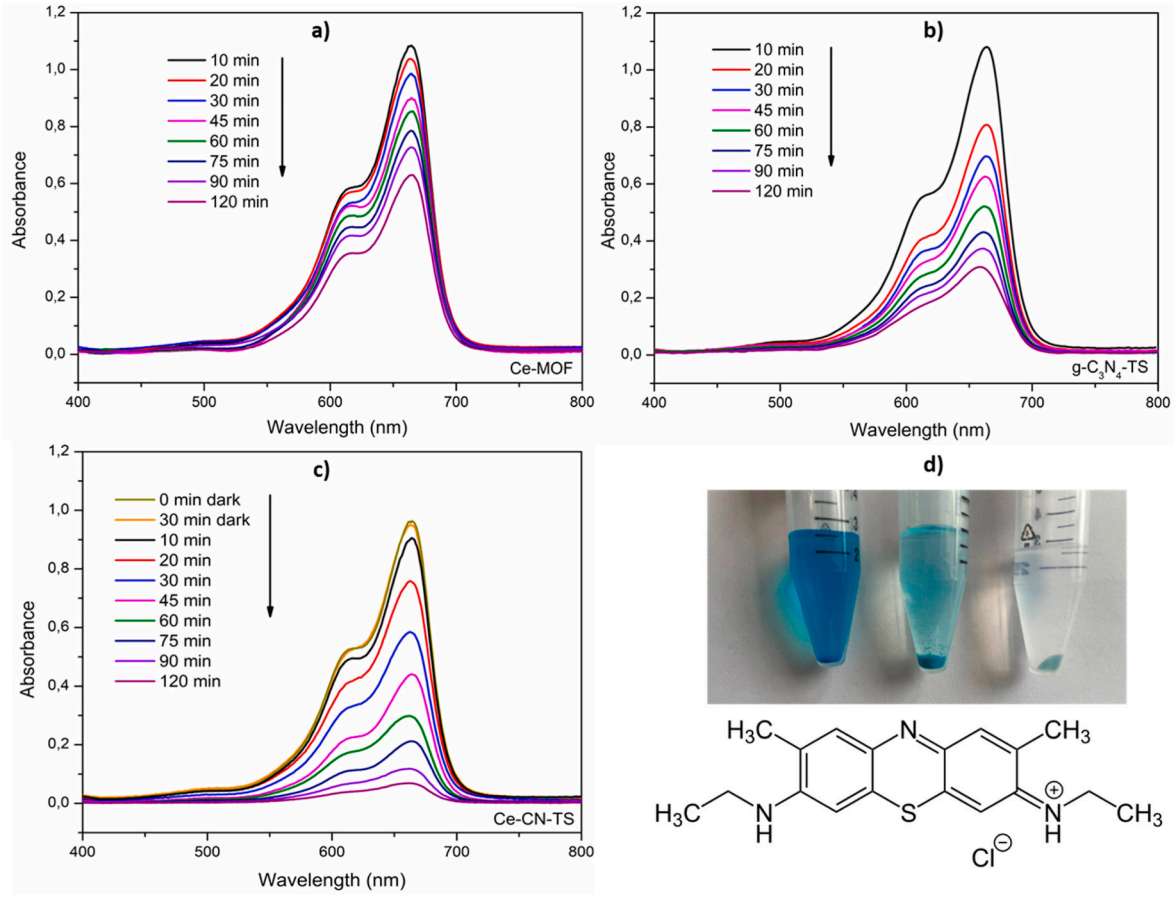


**Fig. 9.** Time-dependent UV–vis spectra of methylene blue suspensions containing **a)** Ce-MOF, **b)** g–$C_3N_4$–TS and **c)** Ce–CN-TS, and **d)** a photograph of the resulting suspensions containing Ce–CN-TS after 30 min, 60 min and 120 min of dye degradation and the molecular formula of MB.

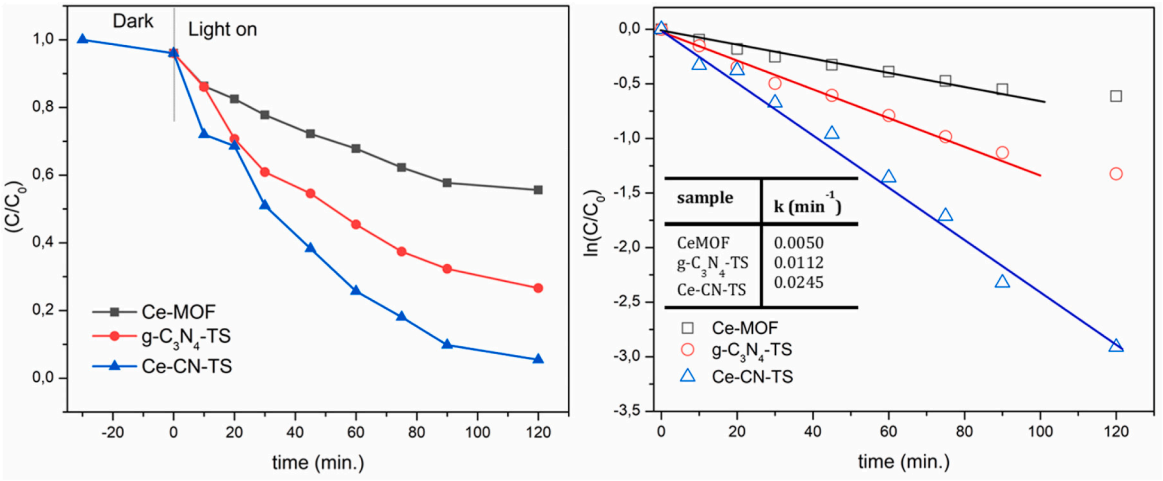


**Fig. 10.** Kinetic curves corresponding to the degradation of methylene blue using Ce-MOF, g–$C_3N_4$–TS and Ce–CN-TS.

0.0265 $min^{-1}$. They also concluded that this increased photocatalytic performance of the hybrid system could be originated from the matched energy level and related heterojunction formation.

Photodegradation of MB was also carried out by Xiao et al. with a similar material under irradiation by visible light to identify the contribution of the dual structure in the heterojunction on the separation of charge carriers [100]. In this case, the degradation efficiency reached 24.8% and 57.0% within 120 min for g-$C_3N_4$ and $NH_2$-MIL-88B (Fe), respectively, and reached 100% for the composite. They showed that the composite structure yielded a much higher degradation efficiency than $NH_2$-MIL-88B(Fe) and g-$C_3N_4$, indicating a synergistic effect of the g-$C_3N_4$/$NH_2$-MIL-88B(Fe) heterojunction for improving the photocatalytic degradation of MB.

Li et al. studied the photocatalytic degradation of MB with a g-$C_3N_4$ hybrid combined with a Zr-based MOF (UiO-66) under visible light irradiation [61]. They reported that the MOF did not exhibit a significant degradation efficiency under visible light as the band gap energy of UiO-66 is 3.6 eV. On the other hand, they also stated that the synergy

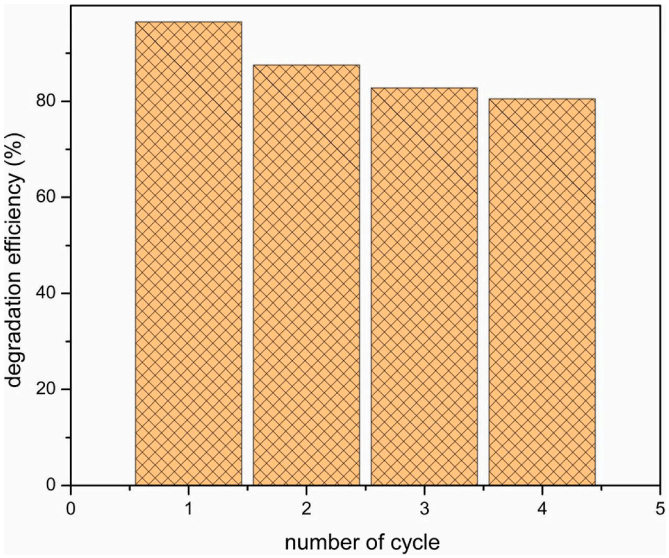


**Fig. 11.** Degradation efficiency of methylene blue degradation as a function of the reaction cycle.

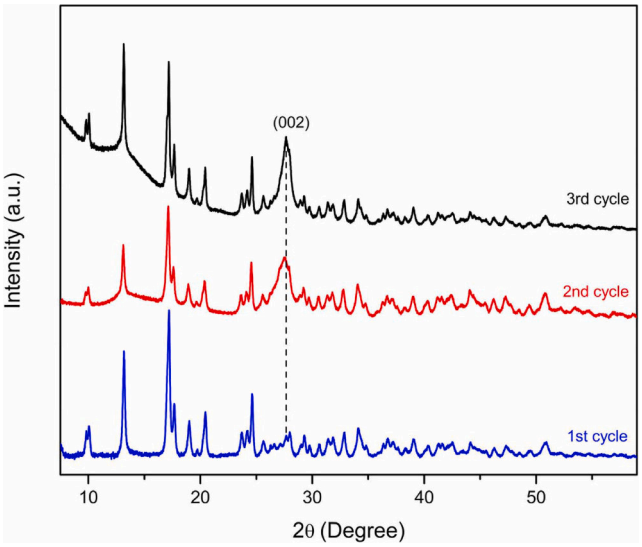


**Fig. 12.** XRD patterns of the Ce–CN-TS composite catalyst after dye degradation cycle.

between UiO-66 and g-$C_3N_4$ reduced the band gap of the hybrid from 3.61 to 2.72 eV, and therefore the photocatalytic efficiency of the hybrid was found to be higher.

The reusability of heterogeneous catalysts is one of the most important aspects for their application performance and commercialization potential. Therefore, the reusability of the Ce–CN-TS composite catalyst was studied in this work, and Fig. 11 shows the degradation efficiency of Ce–CN-TS as a function of the reaction cycle. It was found that the degradation efficiency decreased to a certain extent, namely from 96.5% for the first cycle to 80.5% for the fourth cycle, when the photocatalytic degradation of MB was repeated with the same catalyst under the same reaction conditions. This result shows that the composite catalyst could be used several times without a significant loss in catalytic performance as the degradation efficiency reaches a plateau around 80%.

Coupled with the reusability of the photocatalyst, it should also be stable under the applied reaction conditions. Therefore, the structural stability of the Ce–CN-TS composite catalyst was analyzed by measuring its XRD pattern after the photocatalytic degradation process. Fig. 12 shows the XRD patterns of Ce–CN-TS measured after 1, 2 and 3 cycles of photocatalytic MB degradation. It can be seen that the characteristic diffraction peaks belonging to the crystalline structure of Ce-MOF and the two characteristic peaks of g-$C_3N_4$ are present in all XRD patterns. It is also noteworthy that the intensity of the characteristic inter-planar graphitic stacking (002) peak at ~27° in the composite pattern significantly increased with the number of circles. These XRD results are consistent with the findings reported in Refs. [101,102] and in the references that previously mentioned the structure of Ce(1,3,5-BTC)$(H_2O)_6$ [71,72].

## 4. Conclusions

In this study, hybrid structures were formed between Ce-MOF and g-$C_3N_4$ materials prepared by different synthesis methods. Characterization results showed that both g-$C_3N_4$ and Ce-MOF were successfully synthesized, and that they were subsequently successfully hybridized for the formation of Ce-MOF/g-$C_3N_4$ composites. In light of these characterization results, the composite labeled as Ce–CN-TS was selected as the most suitable composite for photocatalytic dye removal of methylene blue (MB). Through photocatalytic experiments, compared with the bare Ce-MOF and g–$C_3N_4$–TS, the Ce–CN-TS composite structure is certified to possess the highest catalytic activity for the degradation of methylene blue under UV- light. This improvement in the photocatalytic performance can be attributed to the synergistic effect, which promotes charge migration due to the intimate contact between the Ce-MOF and g-$C_3N_4$, which can be inferred from the SEM images. The kinetic curve was found to be in good agreement with the pseudo-first-order kinetic model. Moreover, the reusability of the photocatalyst shows that the composite exhibits good reusability and stability after being used for 4 cycles.

Therefore, this study confirms the high application potential of hybrid g-$C_3N_4$/MOF heterojunctions as efficient photocatalysts for UV light-induced photodegradation, which makes such structures worthy of further investigation.

## Declaration of competing interest

The authors declare that they have no known competing financial interests or personal relationships that could have appeared to influence the work reported in this paper.

## Acknowledgements

Financial support from the MLU Halle-Wittenberg and from the BMBF (grant no.FKZ:03Z22HN11) is greatly acknowledged.

## References

[1] Q. Xia, H. Wang, B.B. Huang, X.Z. Yuan, J.J. Zhang, J. Zhang, L.B. Jiang, T. Xiong, G.M. Zeng, State-of-the-Art advances and challenges of iron-based metal organic frameworks from attractive features, synthesis to multifunctional applications, Small 15 (2019).
[2] H. Yi, D.L. Huang, L. Qin, G.M. Zeng, C. Lai, M. Cheng, S.J. Ye, B. Song, X.Y. Ren, X.Y. Guo, Selective prepared carbon nanomaterials for advanced photocatalytic application in environmental pollutant treatment and hydrogen production, Appl. Catal. B Environ. 239 (2018) 408–424.
[3] J.R. Li, J. Sculley, H.C. Zhou, Metal-organic frameworks for separations, Chem. Rev. 112 (2012) 869–932.
[4] C. Orellana-Tavra, R.J. Marshall, E.F. Baxter, I.A. Lazaro, A. Tao, A.K. Cheetham, R.S. Forgan, D. Fairen-Jimenez, Drug delivery and controlled release from biocompatible metal-organic frameworks using mechanical amorphizationt, J. Mater. Chem. B 4 (2016) 7697–7707.
[5] L. Zhu, X.Q. Liu, H.L. Jiang, L.B. Sun, Metal-organic frameworks for heterogeneous basic catalysis, Chem. Rev. 117 (2017) 8129–8176.
[6] L.E. Kreno, K. Leong, O.K. Farha, M. Allendorf, R.P. Van Duyne, J.T. Hupp, Metal-organic framework materials as chemical sensors, Chem. Rev. 112 (2012) 1105–1125.
[7] D. Lenzen, P. Bendix, H. Reinsch, D. Frohlich, H. Kummer, M. Mollers, P.P. C. Hugenell, R. Glaser, S. Henninger, N. Stock, Scalable green synthesis and full-

scale test of the metal-organic framework CAU-10-H for use in adsorption-driven chillers, Adv. Mater. (2018) 30.
[8] X.Y. Deng, Z.H. Li, H. Garcia, Visible light induced organic transformations using metal-organic-frameworks (MOFs), Chem. Eur J. 23 (2017) 11189–11209.
[9] S.L. Li, Q. Xu, Metal-organic frameworks as platforms for clean energy, Energy Environ. Sci. 6 (2013) 1656–1683.
[10] B.J. Zhu, R.Q. Zou, Q. Xu, Metal-organic framework based catalysts for hydrogen evolution, Adv. Energy Mater. 8 (2018).
[11] W.G. Tu, Y. Xu, S.M. Yin, R. Xu, Rational design of catalytic centers in crystalline frameworks, Adv. Mater. (2018) 30.
[12] W. Meng, Y.F. Zeng, Z.B. Liang, W.H. Guo, C.X. Zhi, Y.X. Wu, R.Q. Zhong, C. Qu, R.Q. Zou, Tuning expanded pores in metal-organic frameworks for selective capture and catalytic conversion of carbon dioxide, ChemSusChem 11 (2018) 3751–3757.
[13] J.D. Xiao, H.L. Jiang, Metal-organic frameworks for photocatalysis and photothermal catalysis, Acc. Chem. Res. 52 (2019) 356–366.
[14] J.D. Xiao, L.L. Han, J. Luo, S.H. Yu, H.L. Jiang, Integration of plasmonic effects and Schottky junctions into metal-organic framework composites: steering charge flow for enhanced visible-light photocatalysis, Angew. Chem., Int. Ed. 57 (2018) 1103–1107.
[15] J. Rocha, L.D. Carlos, F.A.A. Paz, D. Ananias, Luminescent multifunctional lanthanides-based metal-organic frameworks, Chem. Soc. Rev. 40 (2011) 926–940.
[16] B. Liu, W.P. Wu, L. Hou, Y.Y. Wang, Four uncommon nanocage-based Ln-MOFs: highly selective luminescent sensing for $Cu^{2+}$ ions and selective $CO_2$ capture, Chem. Commun. 50 (2014) 8731–8734.
[17] Y. Yu, J.P. Ma, Y.B. Dong, Luminescent humidity sensors based on porous Ln($^{3+}$)-MOFs, CrystEngComm 14 (2012) 7157–7160.
[18] R.D. Shannon, Revised effective ionic-radii and systematic studies of interatomic distances in halides and chalcogenides, Acta Crystallogr. A 32 (1976) 751–767.
[19] M. Kurmoo, Magnetic metal-organic frameworks, Chem. Soc. Rev. 38 (2009) 1353–1379.
[20] J.M. Chapuzet, S. Beauchemin, B. Daoust, J. Lessard, On the mechanism of alcoholysis of allylic and benzylic alcohols and of epoxides in the presence of ceric ammonium nitrate, Tetrahedron 52 (1996) 4175–4180.
[21] T. Takarada, M. Yashiro, M. Komiyama, Catalytic hydrolysis of peptides by cerium(IV), Chem. Eur J. 6 (2000) 3906–3913.
[22] T. Caruso, E. Bedini, C. De Castro, M. Parrilli, Bronsted acidity of ceric ammonium nitrate in anhydrous DMF. The role of salt and solvent in sucrose cleavage, Tetrahedron 62 (2006) 2350–2356.
[23] K. Chondroudis, M.G. Kanatzidis, $[Ce(PSe_4)_4]^{(9-)}$: a highly anionic $Ce^{3+}$ selenophosphate coordination complex, Inorg. Chem. Commun. 1 (1998) 55–57.
[24] J. Danan, C. Denovion, R. Lallement, Magnetic properties of cerium nitride, Solid State Commun. 7 (1969), 1103-1107.
[25] F.W. Tian, C. Fouassier, P. Hagenmuller, Luminescence properties of Ce-$^{3+}$ and Tb-$^{3+}$ in a new family of boron-rich alkaline-earth rare-earth borates, Mater. Res. Bull. 22 (1987) 389–397.
[26] J.W.H. van Krevel, J.W.T. van Rutten, H. Mandal, H.T. Hintzen, R. Metselaar, Luminescence properties of terbium-, cerium-, or europium-doped alpha-sialon materials, J. Solid State Chem. 165 (2002) 19–24.
[27] J. Rossatmignod, P. Burlet, S. Quezel, O. Vogt, Magnetic-ordering in cerium and uranium monopnictides, Physica B C 102 (1980) 237–248.
[28] O. Guillot-Noel, J.T.M. de Haas, P. Dorenbos, C.W.E. van Eijk, K. Kramer, H. U. Gudel, Optical and scintillation properties of cerium-doped $LaCl_3$, $LuBr_3$ and $LuCl_3$, J. Lumin. 85 (1999) 21–35.
[29] Z. Ding, S. Wang, X. Chang, D.H. Wang, T.H. Zhang, Nano-MOF@defected film $C_3N_4$ Z-scheme composite for visible-light photocatalytic nitrogen fixation, RSC Adv. 10 (2020) 26246–26255.
[30] G.F. Liao, C.X. Li, X.Z. Li, B.Z. Fang, Emerging polymeric carbon nitride Z-scheme systems for photocatalysis, Cell Rep. Phys. Sci. 2 (2021).
[31] G. Algara-Siller, N. Severin, S.Y. Chong, T. Bjorkman, R.G. Palgrave, A. Laybourn, M. Antonietti, Y.Z. Khimyak, A.V. Krasheninnikov, J.P. Rabe, U. Kaiser, A. I. Cooper, A. Thomas, M.J. Bojdys, Triazine-based graphitic carbon nitride: a two-dimensional semiconductor, Angew. Chem., Int. Ed. 53 (2014) 7450–7455.
[32] T.M. Su, Q. Shao, Z.Z. Qin, Z.H. Guo, Z.L. Wu, Role of interfaces in two-dimensional photocatalyst for water splitting, ACS Catal. 8 (2018) 2253–2276.
[33] C.L. Tan, X.H. Cao, X.J. Wu, Q.Y. He, J. Yang, X. Zhang, J.Z. Chen, W. Zhao, S. K. Han, G.H. Nam, M. Sindoro, H. Zhang, Recent advances in ultrathin two-dimensional nanomaterials, Chem. Rev. 117 (2017) 6225–6331.
[34] J.X. Low, S.W. Cao, J.G. Yu, S. Wageh, Two-dimensional layered composite photocatalysts, Chem. Commun. 50 (2014) 10768–10777.
[35] O.P. Kumar, M. Ahmad, M.A. Nazir, A. Anum, M. Jamshaid, S.S.A. Shah, A. Rehman, Strategic combination of metal-organic frameworks and $C_3N_4$ for expeditious photocatalytic degradation of dye pollutants, Environ. Sci. Pollut. Res. 29 (2022) 35300–35313.
[36] X.C. Wang, K. Maeda, A. Thomas, K. Takanabe, G. Xin, J.M. Carlsson, K. Domen, M. Antonietti, A metal-free polymeric photocatalyst for hydrogen production from water under visible light, Nat. Mater. 8 (2009) 76–80.
[37] J.S. Zhang, X.F. Chen, K. Takanabe, K. Maeda, K. Domen, J.D. Epping, X.Z. Fu, M. Antonietti, X.C. Wang, Synthesis of a carbon nitride structure for visible-light catalysis by copolymerization, Angew. Chem., Int. Ed. 49 (2010) 441–444.
[38] S. Zhao, J. Xu, M. Mao, L.J. Li, X.H. Li, Protonated g-$C_3N_4$ cooperated with Co-MOF doped with Sm to construct 2D/2D heterojunction for integrated dye-sensitized photocatalytic H-2 evolution, J. Colloid Interface Sci. 583 (2021) 435–447.
[39] W.J. Ong, L.L. Tan, Y.H. Ng, S.T. Yong, S.P. Chai, Graphitic carbon nitride (g-$C_3N_4$)-based photocatalysts for artificial photosynthesis and environmental remediation: are we a step closer to achieving sustainability? Chem. Rev. 116 (2016) 7159–7329.
[40] Y.L. Li, X.F. Xu, J.S. Wang, W. Luo, Z.P. Zhang, X. Cheng, J.S. Wu, Y.L. Yang, G. Chen, S.R. Sun, L.Z. Wang, Post-Redox Engineering Electron Configurations of Atomic Thick $C_3N_4$ Nanosheets for Enhanced Photocatalytic Hydrogen Evolution, Appl Catal B-Environ (2020) 270.
[41] K.H. Sun, J. Shen, Q.Q. Liu, H. Tang, M.Y. Zhang, S. Zulfiqar, C.S. Lei, Synergistic effect of Co(II)-hole and Pt-electron cocatalysts for enhanced photocatalytic hydrogen evolution performance of P-doped g-$C_3N_4$, Chin. J. Catal. 41 (2020) 72–81.
[42] L.T. Ma, H.Q. Fan, K. Fu, S.H. Lei, Q.Z. Hu, H.T. Huang, G.P. He, Protonation of graphitic carbon nitride (g-$C_3N_4$) for an electrostatically self-assembling Carbon@ g-$C_3N_4$ core shell nanostructure toward high hydrogen evolution, ACS Sustain. Chem. Eng. 5 (2017) 7093–7103.
[43] Y.Z. Hong, L.Y. Wang, E.L. Liu, J.H. Chen, Z.G. Wang, S.Q. Zhang, X. Lin, X. X. Duan, J.Y. Shi, A curly architectured graphitic carbon nitride (g-$C_3N_4$) towards efficient visible-light photocatalytic $H_2$ evolution, Inorg. Chem. Front. 7 (2020) 347–355.
[44] S.E. Guo, Z.P. Deng, M.X. Li, B.J. Jiang, C.G. Tian, Q.J. Pan, H.G. Fu, Phosphorus-Doped carbon nitride tubes with a layered micro-nanostructure for enhanced visible-light photocatalytic hydrogen evolution, Angew. Chem., Int. Ed. 55 (2016) 1830–1834.
[45] Y. Wang, X.C. Wang, M. Antonietti, Polymeric graphitic carbon nitride as a heterogeneous organocatalyst: from photochemistry to multipurpose catalysis to sustainable chemistry, Angew. Chem., Int. Ed. 51 (2012) 68–89.
[46] Z. Durmus, A.W. Maijenburg, A review on graphitic carbon nitride (g-$C_3N_4$) – metal organic framework (MOF) heterostructured photocatalyst materials for photo(electro)chemical hydrogen evolution, Int. J. Hydrogen Energy 47 (2022) 36784–36813.
[47] H.Y. Xie, Y.Z. Wei, J.K. Li, S.S. Wang, H.J. Li, Y.F. Zhao, M. Zhao, X.F. Chen, In-situ exfoliation of graphitic carbon nitride with metal-organic framework via a sonication-assisted approach for dispersive solid-phase extraction of perfluorinated compounds in drinking water samples, J. Chromatogr. A (2020) 1625.
[48] H.Q. Li, Y.X. Liu, X. Gao, C. Fu, X.C. Wang, Facile synthesis and enhanced visible-light photocatalysis of graphitic carbon nitride composite semiconductors, ChemSusChem 8 (2015) 1189–1196.
[49] N.M. Mahmoodi, Surface modification of magnetic nanoparticle and dye removal from ternary systems, J. Ind. Eng. Chem. 27 (2015) 251–259.
[50] N.M. Mahmoodi, Photocatalytic ozonation of dyes using multiwalled carbon nanotube, J. Mol. Catal. Chem. 366 (2013) 254–260.
[51] S.M. Lam, J.C. Sin, A.R. Mohamed, A review on photocatalytic application of g-$C_3N_4$/semiconductor (CNS) nanocomposites towards the erasure of dyeing wastewater, Mater. Sci. Semicond. Process. 47 (2016) 62–84.
[52] B. Hayati, N.M. Mahmoodi, Modification of activated carbon by the alkaline treatment to remove the dyes from wastewater: mechanism, isotherm and kinetic, Desalination Water Treat. 47 (2012) 322–333.
[53] N.M. Mahmoodi, Photocatalytic Degradation of Dyes Using Carbon Nanotube and Titania Nanoparticle, Water Air Soil Pollut. 224 (2013) 1612.
[54] N.M. Mahmoodi, Synthesis of magnetic carbon nanotube and photocatalytic dye degradation ability, Environ. Monit. Assess. 186 (2014) 5595–5604.
[55] N.M. Mahmoodi, M. Arami, Numerical finite volume modeling of dye decolorization using immobilized titania nanophotocatalysis, Chem. Eng. J. 146 (2009) 189–193.
[56] J.C. Tong, L. Zhang, F. Li, M.M. Li, S.K. Cao, An efficient top-down approach for the fabrication of large-aspect-ratio g-$C_3N_4$ nanosheets with enhanced photocatalytic activities, Phys. Chem. Chem. Phys. 17 (2015) 23532–23537.
[57] Z.H. Huang, H. Chen, L. Zhao, W. Fang, X. He, W.X. Li, P. Tian, In suit inducing electron-donating and electron-withdrawing groups in carbon nitride by one-step $NH_4Cl$-assisted route: a strategy for high solar hydrogen production efficiency, Environ. Int. 126 (2019) 289–297.
[58] H.Y. Niu, W.J. Zhao, H.Z. Lv, Y.L. Yang, Y.Q. Cai, Accurate design of hollow/tubular porous g-$C_3N_4$ from melamine-cyanuric acid supramolecular prepared with mechanochemical method, Chem. Eng. J. 411 (2021) 128400.
[59] J. Barrio, M. Volokh, M. Shalom, Polymeric carbon nitrides and related metal-free materials for energy and environmental applications, J. Mater. Chem. 8 (2020) 11075–11116.
[60] L.F. Li, J.H. Zhang, Q. Zhang, X.H. Wang, W.L. Dai, Superior sponge-like carbon self-doping graphitic carbon nitride nanosheets derived from supramolecular pre-assembly of a melamine-cyanuric acid complex for photocatalytic $H_2$ evolution, Nanotechnology 32 (2021) 155604.
[61] Y. Zhang, J.B. Zhou, Q.Q. Feng, X. Chen, Z.S. Hu, Visible light photocatalytic degradation of MB using UiO-66/g-$C_3N_4$ heterojunction nanocatalyst, Chemosphere 212 (2018) 523–532.
[62] J. Xu, L.W. Zhang, R. Shi, Y.F. Zhu, Chemical exfoliation of graphitic carbon nitride for efficient heterogeneous photocatalysis, J. Mater. Chem. 1 (2013) 14766–14772.
[63] Y.H. Li, C.F. Gao, J. Jiao, J.S. Cui, Z.A. Li, Q. Song, Selective adsorption of metal-organic framework toward methylene blue: behavior and mechanism, ACS Omega 6 (2021) 33961–33968.
[64] A. El-Kebir, A. Harrane, M. Belbachir, Protonated montmorillonite clay used as green non-toxic catalyst for the synthesis of biocompatible polyglycidol, Arabian J. Sci. Eng. 41 (2016) 2179–2184.

[65] A.P. Singh, P. Arora, S. Basu, B.R. Mehta, Graphitic carbon nitride based hydrogen treated disordered titanium dioxide core-shell nanocatalyst for enhanced photocatalytic and photoelectrochemical performance, Int. J. Hydrogen Energy 41 (2016) 5617–5628.
[66] S.C. Yan, Z.S. Li, Z.G. Zou, Photodegradation performance of g-$C_3N_4$ fabricated by directly heating melamine, Langmuir 25 (2009) 10397–10401.
[67] A. Thomas, A. Fischer, F. Goettmann, M. Antonietti, J.O. Muller, R. Schlogl, J. M. Carlsson, Graphitic carbon nitride materials: variation of structure and morphology and their use as metal-free catalysts, J. Mater. Chem. 18 (2008) 4893–4908.
[68] Z.H. Chen, P. Sun, B. Fan, Q. Liu, Z.G. Zhang, X.M. Fang, Textural and electronic structure engineering of carbon nitride via doping with pi-deficient aromatic pyridine ring for improving photocatalytic activity, Appl. Catal. B Environ. 170 (2015) 10–16.
[69] G.G. Zhang, J.S. Zhang, M.W. Zhang, X.C. Wang, Polycondensation of thiourea into carbon nitride semiconductors as visible light photocatalysts, J. Mater. Chem. 22 (2012) 8083–8091.
[70] Y.H. Liang, R. Shang, J.R. Lu, W.J. An, J.S. Hu, L. Liu, W.Q. Cui, 2D MOFs enriched g-$C_3N_4$ nanosheets for highly efficient charge separation and photocatalytic hydrogen evolution from water, Int. J. Hydrogen Energy 44 (2019) 2797–2810.
[71] G.J. Zeng, Y. Chen, L. Chen, P.X. Xiong, M.D. Wei, Hierarchical cerium oxide derived from metal-organic frameworks for high performance supercapacitor electrodes, Electrochim. Acta 222 (2016) 773–780.
[72] Y.H. Xiong, S.H. Chen, F.G. Ye, L.J. Su, C. Zhang, S.F. Shen, S.L. Zhao, Synthesis of a mixed valence state Ce-MOF as an oxidase mimetic for the colorimetric detection of biothiols, Chem. Commun. 51 (2015) 4635–4638.
[73] N. Tian, Y.H. Zhang, X.W. Li, K. Xiao, X. Du, F. Dong, G.I.N. Waterhouse, T. R. Zhang, H.W. Huang, Precursor-reforming protocol to 3D mesoporous g-$C_3N_4$ established by ultrathin self-doped nanosheets for superior hydrogen evolution, Nano Energy 38 (2017) 72–81.
[74] P. Niu, L.L. Zhang, G. Liu, H.M. Cheng, Graphene-like carbon nitride nanosheets for improved photocatalytic activities, Adv. Funct. Mater. 22 (2012) 4763–4770.
[75] F. Chang, Y.C. Xie, C.L. Li, J. Chen, J.R. Luo, X.F. Hu, J.W. Shen, A facile modification of g-$C_3N_4$ with enhanced photocatalytic activity for degradation of methylene blue, Appl. Surf. Sci. 280 (2013) 967–974.
[76] Y.Y. Huang, D. Li, Z.Y. Fang, R.J. Chen, B.F. Luo, W.D. Shi, Controlling carbon self-doping site of g-$C_3N_4$ for highly enhanced visible-light-driven hydrogen evolution, Appl. Catal. B Environ. 254 (2019) 128–134.
[77] B. Yue, Q.Y. Li, H. Iwai, T. Kako, J.H. Ye, Hydrogen production using zinc-doped carbon nitride catalyst irradiated with visible light, Sci. Technol. Adv. Mater. 12 (2011), 034401.
[78] Y.Y. Li, Y. Si, B.X. Zhou, T. Huang, W.Q. Huang, W.Y. Hu, A.L. Pan, X.X. Fan, G. F. Huang, Interfacial charge modulation: carbon quantum dot implanted carbon nitride double-deck nanoframes for robust visible-light photocatalytic tetracycline degradation, Nanoscale 12 (2020) 3135–3145.
[79] S. Martha, A. Nashim, K.M. Parida, Facile synthesis of highly active g-$C_3N_4$ for efficient hydrogen production under visible light, J. Mater. Chem. 1 (2013) 7816–7824.
[80] K. Akaike, K. Aoyama, S. Dekubo, A. Onishi, K. Kanai, Characterizing electronic structure near the energy gap of graphitic carbon nitride based on rational interpretation of chemical analysis, Chem. Mater. 30 (2018) 2341–2352.
[81] T.S. Miller, A.B. Jorge, T.M. Suter, A. Sella, F. Cora, P.F. McMillan, Carbon nitrides: synthesis and characterization of a new class of functional materials, Phys. Chem. Chem. Phys. 19 (2017) 15613–15638.
[82] R. Zhang, J.X. Dong, G.L. Gao, X.L. Wang, Y.F. Yao, Facile synthesis of amorphous $C_3N_4Zn_xO_y$ (x, y=0.32-1.10) with high photocatalytic efficiency for antibiotic degradation, Catalysts 10 (2020) 514.
[83] Y.G. Xu, M. Xie, S.Q. Huang, H. Xu, H.Y. Ji, J.X. Xia, Y.P. Li, H.M. Li, High yield synthesis of nano-size g-$C_3N_4$ derivatives by a dissolve-regrowth method with enhanced photocatalytic ability, RSC Adv. 5 (2015) 26281–26290.
[84] Q.L. Xu, B. Cheng, J.G. Yu, G. Liu, Making co-condensed amorphous carbon/g-$C_3N_4$ composites with improved visible-light photocatalytic $H_2$ production performance using Pt as cocatalyst, Carbon 118 (2017) 241–249.
[85] L.Y. Wang, Y.Z. Hong, E.L. Liu, X.X. Duan, X. Lin, J.Y. Shi, A bottom-up acidification strategy engineered ultrathin g-$C_3N_4$ nanosheets towards boosting photocatalytic hydrogen evolution, Carbon 163 (2020) 234–243.
[86] Q.H. Liang, Z. Li, Z.H. Huang, F.Y. Kang, Q.H. Yang, Holey graphitic carbon nitride nanosheets with carbon vacancies for highly improved photocatalytic hydrogen production, Adv. Funct. Mater. 25 (2015) 6885–6892.
[87] A.G. Rashidizadeh, H. Rezazadeh Z, Improved visible-light photocatalytic activity of g-$C_3N_4$/$CuWO_4$ nanocomposite for degradation of methylene blue, Proceedings 41 (2019) 43–46.
[88] W.N. Xing, G. Chen, C.M. Li, Z.H. Han, Y.D. Hu, Q.Q. Meng, Doping effect of non-metal group in porous ultrathin g-$C_3N_4$ nanosheets towards synergistically improved photocatalytic hydrogen evolution, Nanoscale 10 (2018) 5239–5245.
[89] C.Y. Wang, K. Li, P.J. Ji, Using taurine to increase mesopores in Ce-based metal-organic framework for enhancing the production of 5-hydroxymethylfurfural and 5-ethoxymethylfurfural from fructose, J. Chem. Technol. Biotechnol. 96 (2021) 163–171.
[90] S. Maiti, A. Pramanik, S. Mahanty, Extraordinarily high pseudocapacitance of metal organic framework derived nanostructured cerium oxide, Chem. Commun. 50 (2014) 11717–11720.
[91] Y.C. Tsai, J. Lee, E. Kwon, C.W. Huang, N.N. Huy, S.M. You, P.S. Hsu, W.D. Oh, K. Y.A. Lin, Enhanced catalytic soot oxidation by Ce-based MOF-derived ceria nano-bar with promoted oxygen vacancy, Catalysts 11 (2021) 1128.
[92] X.J. Wang, X. Tian, F.T. Li, Y.P. Li, J. Zhao, Y.J. Hao, Y. Liu, Synchronous surface hydroxylation and porous modification of g-$C_3N_4$ for enhanced photocatalytic $H_2$ evolution efficiency, Int. J. Hydrogen Energy 41 (2016) 3888–3895.
[93] A. Ranganathan, V.R. Pedireddi, C.N.R. Rao, Hydrothermal synthesis of organic channel structures: 1 : 1 hydrogen-bonded adducts of melamine with cyanuric and trithiocyanuric acids, J. Am. Chem. Soc. 121 (1999) 1752–1753.
[94] E.G. Gillan, Synthesis of nitrogen-rich carbon nitride networks from an energetic molecular azide precursor, Chem. Mater. 12 (2000) 3906–3912.
[95] Y.J. Cui, J.S. Zhang, G.G. Zhang, J.H. Huang, P. Liu, M. Antonietti, X.C. Wang, Synthesis of bulk and nanoporous carbon nitride polymers from ammonium thiocyanate for photocatalytic hydrogen evolution, J. Mater. Chem. 21 (2011) 13032–13039.
[96] H.Y. Nie, M. Ou, Q. Zhong, S.L. Zhang, L.M. Yu, Efficient visible-light photocatalytic oxidation of gaseous NO with graphitic carbon nitride (g-$C_3N_4$) activated by the alkaline hydrothermal treatment and mechanism analysis, J. Hazard Mater. 300 (2015) 598–606.
[97] B. Fang, Z. Xing, D. Sun, Z. Li, W. Zhou, Hollow semiconductor photocatalysts for solar energy conversion, Adv. Powder Mater. 1 (2022), 100021.
[98] Z.D. Lei, Y.C. Xue, W.Q. Chen, L. Li, W.H. Qiu, Y. Zhang, L. Tang, The influence of carbon nitride nanosheets doping on the crystalline formation of MIL-88B(Fe) and the photocatalytic activities, Small 14 (2018).
[99] Z. Durmus, B.Z. Kurt, A. Durmus, Synthesis and characterization of graphene oxide/zinc oxide (GO/ZnO) nanocomposite and its utilization for photocatalytic degradation of basic fuchsin dye, ChemistrySelect 4 (2019) 271–278.
[100] X.Y. Li, Y.H. Pi, L.Q. Wu, Q.B. Xia, J.L. Wu, Z. Li, J. Xiao, Facilitation of the visible light-induced Fenton-like excitation of $H_2O_2$ via heterojunction of g-$C_3N_4$/$NH_2$-Iron terephthalate metal-organic framework for MB degradation, Appl. Catal. B Environ. 202 (2017) 653–663.
[101] K. Liu, H.P. You, G. Jia, Y.H. Zheng, Y.J. Huang, Y.H. Song, M. Yang, L.H. Zhang, H.J. Zhang, Hierarchically nanostructured coordination polymer: facile and rapid fabrication and tunable morphologies, Cryst. Growth Des. 10 (2010) 790–797.
[102] A.A. Ibrahim, A. Lin, F.M. Zhang, K.M. AbouZeid, M.S. El-Shall, Palladium nanoparticles supported on a metal-organic framework-partially reduced graphene oxide hybrid for the catalytic hydrodeoxygenation of vanillin as a model for biofuel upgrade reactions, ChemCatChem 9 (2017) 469–480.